이학박사 학위논문

Structure study on multiferroic materials: Hexagonal manganites and $PbFe_{0.5}Nb_{0.5}O_3$

다중강성 물질의 구조연구: 육방정계 망간산화물과 $PbFe_{0.5}Nb_{0.5}O_3$

2018년 2월

서울대학교 대학원

물리천문학부 물리학전공

심 하 성

Structure study on multiferroic materials: Hexagonal manganites and $PbFe_{0.5}Nb_{0.5}O_3$

지도 교수 박 제 근

이 논문을 이학박사 학위논문으로 제출함
2018년 2월

서울대학교 대학원
물리천문학부 물리학전공
심 하 성

심하성의 이학박사 학위논문을 인준함
2017년 12월

위 원 장 _____ (인)

부위원장 _____ (인)

위 원 _____ (인)

위 원 _____ (인)

위 원 _____ (인)

Abstract

Among multiferroic materials that have both ferroelectricity and magnetism, the properties of hexagonal manganite ($RMnO_3$) and perovskite type $PbFe_{0.5}Nb_{0.5}O_3$ were studied by means of a structure analysis. For h-$RMnO_3$ having a unique two dimensional triangular lattice, the structural transition path from the paraelectric $P6_3/mmc$ structure to the ferroelectric $P6_3cm$ structure was studied. Not using normal Rietveld refinement but instead with a mode analysis using the peak intensity, we found that the structural transition is a single transition and that the R-O_P displacement mode resembles a first-order transition, while the MnO_5 tilting mode and the polarization mode behave as second order transitions. Ferroelectric transitions and magnetic property changes were also studied in $YMnO_3$ after doping non-magnetic Al and Ga ion into Mn sites. The R-O_P displacement mode, which shows first-order transition behavior, gradually changes to a smooth second-order transition as the Al doping ratio gets increased. Because Al ions are smaller than Mn ions, the local strain induced by the size difference is the likely cause of this outcome. We also note that there are the decrease in magnetic transition temperature, low temperature ferromagnetism and low energy excitation with the doping ratio of Al and Ga.

The structure of perovskite type $PbFe_{0.5}Nb_{0.5}O_3$ was studied by both high-resolution neutron diffraction and total scattering methods. Our diffraction study, the structure confirmed Cm structure and by a local structure study, we also found that the local structure showed Pb displacement and oxygen disorder even above the structural transition temperature. In this systematic study of multiferroic materials, I suggest a new methods of structural analysis that will be helpful to those undertaking structural studies of other multiferroic materials.

Keywords: triangular antiferromagnet, $RMnO_3$, $PbFe_{0.5}Nb_{0.5}O_3$
Student Number: 2011-20408

Contents

List of Tables

List of Figures

1. Introduction

1.1 Multiferroics and structural analysis

There are four phases of materials: gas, liquid, solid and plasma. Solids whose constituents are arranged in a highly ordered microscopic structure, form a crystal lattice that extends in all directions, referred to as crystals. Crystals that exhibit more than one of the primary ferroic order parameters are known as multiferroic materials.

What I studied for this thesis are multiferroic materials having ferroelectricity and magnetism as show in figure 1.1. Major issues include spin-lattice coupling, broken inversion symmetry, Dzyaloshinskii-Moriya interaction and spin-orbit coupling. $BiFeO_3$, $PbVO_3$, $Lu_2Fe_2O_4$, $RMnO_3$ and CuO are well-known examples of multiferroic materials.

Structure analysis methods play an important role in the study of multiferroic materials. Essentially, a structural analysis provides information about how atoms are arranged in a unit cell. Displacement during a structural transition induces ferroelectricity, hence, research on different structures is helpful to improve our understanding of the behavior of ferroelectricity by examining the atom positions depending on the temperature (figure 1.2).

Magnetic structural analysis methods also increase our understanding of magnetic behavior by providing information about how magnetic moments are ordered. Neutron diffraction experiments are used in magnetic structural studies, representing the starting point when studying magnetic properties.

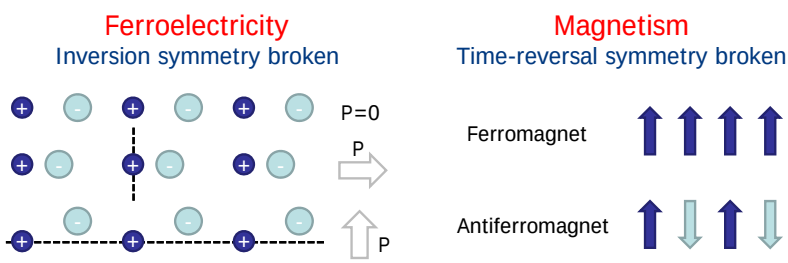

Figure 1.1: Multiferroic materials

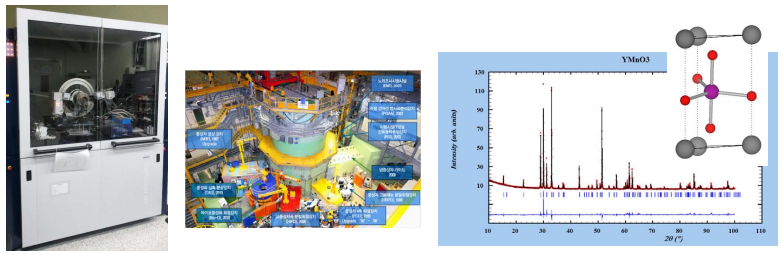

Figure 1.2: Structural analysis

Multiferroic materials are materials with more than one order parameter, implying that coupling between them is important. Magnetic transitions can induce structural changes and structural transitions can also induce magnetic structural change. This type of magneto-electric coupling can be studied thoroughly by crystal and magnetic structural analysis methods.

1.2 Outline of thesis

In chapter 2, I introduce the experimental methods used in the sample synthesis and structural analysis as mainly investigated here. The sample synthesis parts include solid-state reactions and floating-zone crystal growth characteristics. The structural analysis parts include the global structural analysis, local structural analysis and magnetic structural analysis.

In the following chapters, I discuss hexagonal manganite $RMnO_3$, a well-known multiferroic material system. A h-$RMnO_3$ has a unique two-dimensional triangular lattice with the MnO_5 polyhedral. It undergoes a ferroelectric transition around 1200 K and an antiferromagnetic transition due to Mn atoms around 70 K. In chapter 3, I discuss the path in which h-$RMnO_3$(R = In, Y, Ho - Lu) follows during the ferroelectric transition from the paraelectric $P6_3/mmc$ structure to the ferroelectric $P6_3cm$ structure. In chapter 4, how ferroelectric transitions would change upon doping with Al or Ga into the Mn sites of h-$YMnO_3$ will be discussed. In chapter 5, the non-magnetic impurity effects of the physical properties and the magnetic structure on the magnetic triangular lattice upon

doping with Al or Ga into the Mn sites of h-$YMnO_3$ are discussed.

Finally I discuss perovskite type $Pb(Fe_{0.5}Nb_{0.5})O_3$ in chapter 6. This materials is of interest given that it is a relaxor multiferroic materials with a high dielectric constant. With both high-resolution neutron diffraction studies and total scattering methods, I investigate and determine its global and local structures.

2. Experimental techniques

The experimental techniques that used in this thesis are explained in this chapter. Methods for the sample synthesis and structural analysis will be discussed.

2.1 Sample synthesis

Crystals are solid arranged in a highly ordered microscopic structure, forming a crystal lattice. The existence of crystal is important in the beginning and during the process. The quality and size of the crystals are also important. In this section, a solid-state reaction (sub section 2.1.1) and floating-zone crystal growth (sub section 2.1.2) will be explained.

2.1.1 Solid-state reaction

The Solid-state reaction is the most widely used method for preparing polycrystalline samples. Polycrystalline samples are powders with crystals normally less than 10 μm in size. They are used for powder X-ray or neutron diffraction experiments or other physical property measurements.

Figure 2.1 shows a basic diagram of the solid state reaction. Raw materials are mixed at a stoichiometric ratio. When the raw materials are volatile, a few percentages are added to compensate for evaporation. These mixed powders are then heated after being pelletized or a powder form. Heating the samples increases the reactivity and decreases the

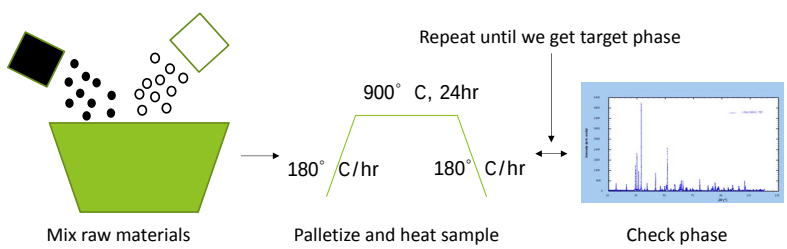

Figure 2.1: Solid state reaction.

reaction time. Furnaces are used to heat the samples, and pelletizing serves to increase the area of contact between the raw materials and reduce the time for synthesis.

Several parameters, such as the ratio of the raw materials, the heating time and the temperature affects the sample synthesis process. Even the atmosphere, pressure, mixing time, pre-treatment process and oxidation state of the raw materials affect the synthesis process. For example, choosing MnO, MnO_2 or Mn_2O_3 affects the impurity amount when sintering $YMnO_3$.

There is no special method used to establish the synthesis conditions for a specific sample. By comparing the sintering condition with those of intermetallic other similar materials, methods are finalized by trials and errors with a checking with XRD for every trial. How much the sintering condition is finalized will determine the quality of poly crystalline samples.

2.1.2 Floating-zone crystal growth

If we can grow large single crystals, characteristics according to the direction of the sample can be obtained, which offers more information than an experiment using poly crystalline samples. Large single crystals are useful when conducting elastic neutron diffraction experiments; inelastic neutron scattering experiments; or other physical properties measurements such as magnetism, heat capacity, thermal expansion and resistivity measurements.

The optical floating-zone furnace technique allows the control of the atmosphere around the material during growth, grows very large crystals, and avoids contamination from the crucible or other containers by doing away with them entirely. Floating-zone growth is particularly effective for oxides.

Figure 2.2(a) shows an image of a floating-zone furnace of the type used here to grow the crystals (model: FZ-T-10000-H-VII-VPO-PC, Crystal Systems Corporation). It has four halogen lamps and mirrors to melt the samples (Fig. 2.2(b)) and the growth process can be monitored in real time(Fig. 2.2(c)).

Figure 2.2(d) shows a schematics of a floating-zone furnace. We pre-

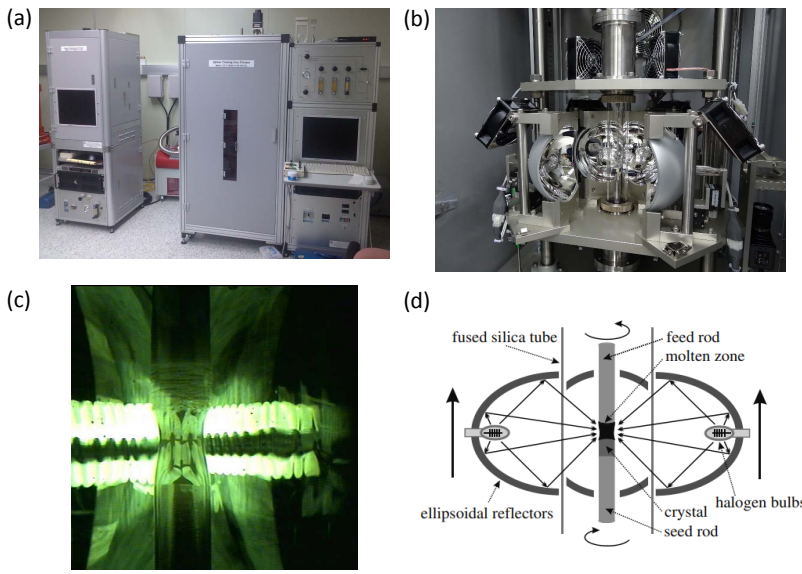

Figure 2.2: (a) Floating zone furnace. (b) We used 4 mirror floating zone furnace. (c) Image during growing single crystals. (d) Schematics diagram of floating zone furnace [1]

pared the feed rod and the seed rod by a solid-state reaction(Sub section 2.1.1), and they are connected with melting zone in which melting is done with light. Mirrors are then moved upward so that the samples are stacked and grow on the seed rod parts. The normal growth speed is 2 mm/hr.

Figure 2.3 shows the growth of several single crystals. We succeeded in growing a wide range of hexagonal manganite as well as orthoferrites and other multiferroic oxides. The grown crystals are then checked and oriented with a Laue machine, as shown in figure 2.4, and subsequently cut along special orientations. The samples were then used for several physical property measurements, structural analysis or other types of measurements.

2.2 Structural analysis

A structural analysis is a basic tool for analyzing how atoms are arranged in a unit cell. Atomic displacements from symmetrical positions

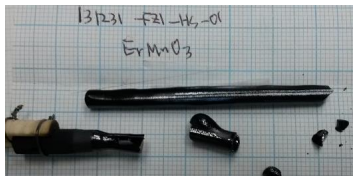

$ErMnO_3$

$YMnO_3$

$LaFeO_3$

$YMn_{0.75}Ga_{0.25}O_3$

Figure 2.3: Single crystals grown by floating zone furnace

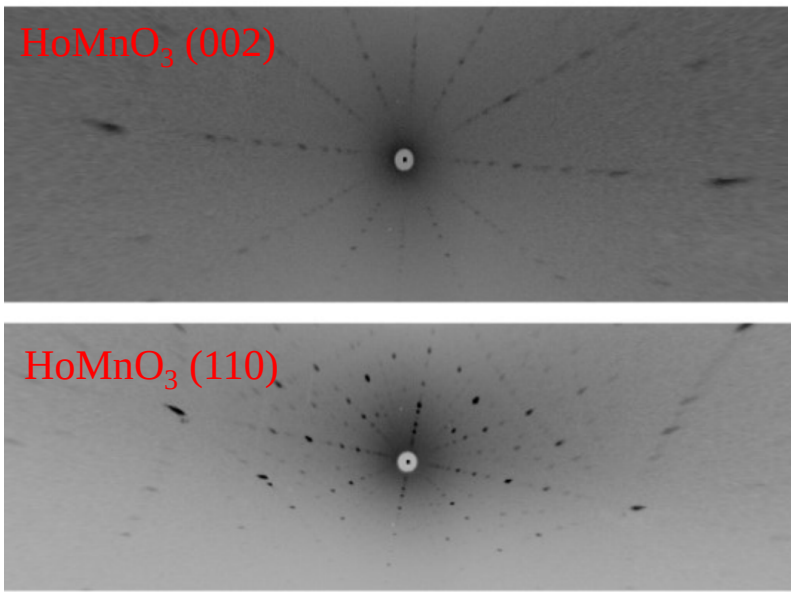

Figure 2.4: Laue image of grown crystals. Orientation were checked for other physical properties measurements.

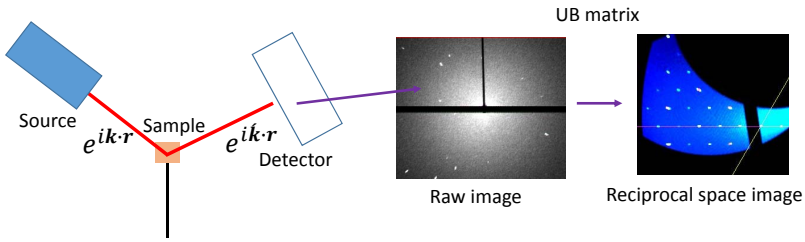

Figure 2.5: Schematics diagram of single crystal XRD measurements and raw data.

in ferroelectric materials, magnetic structures, and atomic movements due to magnetoelectric coupling can be analyzed. The global structural analysis and local structural analysis are explained here.

2.2.1 Global structure analysis

The global structural analysis, also known as a long-range structural analysis is the most widely used means of structural analysis. It is possible to determine lattice constants, atom position and temperature parameters using this process. Source beams, X-rays or neutrons are reflected or transmitted in samples, and detector reads the beam from the samples depending on the angle or time.

A basic drawing of a single crystal X-ray diffractometer is shown in figure 2.5. The beam from the source is diffracted on the samples and then goes to the detector. Images measured in the detector are converted to the k-space by considering the machine geometry. K-space images are then mapped to a reciprocal space image with the UB matrix, which contains information about the sample unit cell and orientation when measured.

$$F = \int dV n(\boldsymbol{r}) exp\left[i(\boldsymbol{k} - \dot{\boldsymbol{k}}) \cdot \boldsymbol{r}\right],$$

The equation above shows the structural factor F as obtained from the k space. The structural factor, for the case of an X-ray beam, can be calculated by the local electron density $n(\boldsymbol{r})$, and the geometry of the incident beam $e^{i\boldsymbol{k}\cdot\boldsymbol{r}}$ and reflected beam $e^{i\dot{\boldsymbol{k}}\cdot\boldsymbol{r}}$. We obtain two types of information, the position and the intensity of the peaks, in this manner.

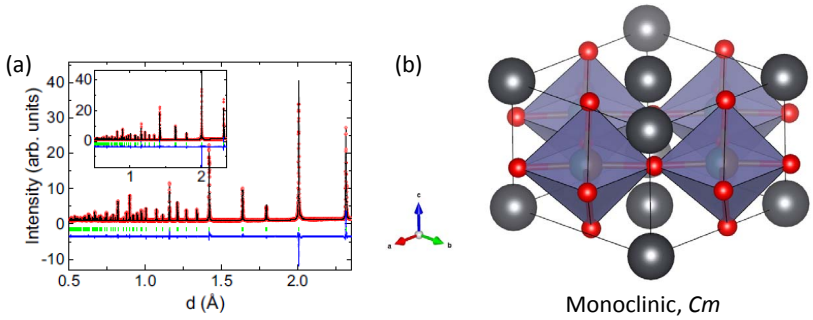

Figure 2.6: (a) Refinement results and (b) structure.

Powder diffraction is similar. Figure 2.6(a) show image of time-of-flight neutron powder diffraction data. All types of directional information are added; hence with powder diffraction, we can only determine the intensity depending on one geometric parameter, the angle or the time. We can thus acquire the d-spacing and the peak intensity.

The peaks' positions are related to the d-spacing and are thus related to the lattice constants of the samples. The machine resolution is also related to the peaks' width. The peak intensity values are related to the atom position and are related to the flux intensity of the beam and the degree of sensitivity of the detector.

Rietveld refinement refers to the process of minimizing the difference between the observed results and the calculated results. Figure 2.6(a) shows the measured (red circle), calculated (black line) and difference (blue line) in the data.

$$M = \sum_i W_i \left[y_i^{obs} - \frac{1}{c} y_i^{calc} \right]^2$$

W_i is the statistical weight and Rietveld refinement minimizes M by least-scale fitting. With this process, we can ascertain the structure of the unit cell, as shown in figure 2.6(b).

Figure 2.7 shows a powder X-ray diffractometer and a neutron facility both of which are widely used for structural analysis.

There are several reasons for using both source types, i.e., X-rays and neutrons. As shown in figure 2.8, the scattering form factor differ depending on the source. The form factor for X-rays increases as the

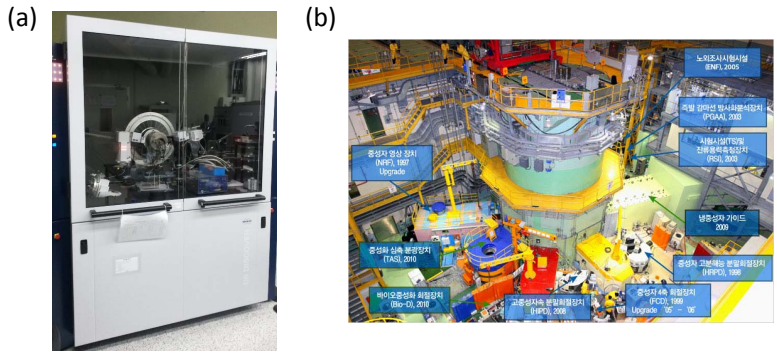

Figure 2.7: (a) Powder X-ray diffractometer and (b) neutron facility.

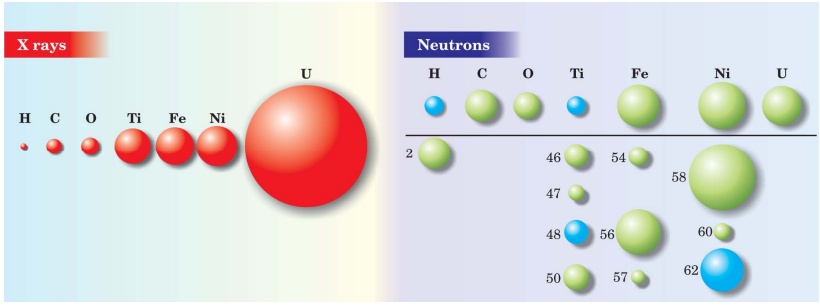

Figure 2.8: A comparison of X -ray and neutron scattering cross sections [2].

atom number increases, whereas this is not the case for the form factor for neutron. Therefore, neutrons are feasible for observing light atoms or isotope effects. The beam flux of X-ray source is quite high; hence using an X-ray source can lead to better resolutions than a neutron source, and neutron experiments require a large amount of sample due to the low flux. We can easily gain access to X-ray source, even at a regular lab, but a large facility is required for a neutron source. Neutron sources have the advantage of being able to examine magnetic signals. The two sources have their own advantages, and thus both sources are used for a structural analysis.

2.2.2 Local structural analysis

The structure is determined solely based upon the information provided by the position and intensity of the Bragg peaks, while additional information regarding the degree of deviation from a perfect lattice is obtained through the study of the diffuse scattering characteristics [3]. This approach makes sense when the deviations are small, whereas when the structure is extensively disordered it fails in practice [3].

An alternative approach which considers both the Bragg peaks and diffuse scattering on an equal basis is the total scattering technique. Data from the throughout reciprocal space over a wide range of Q-values is Fourier-transformed into real space [3].

The Fourier-transform equation is as follows. The experimentally obtained $S(Q)$ is Fourier transformed into real space to obtain the atomic pair distribution function $G(r)$, as follows:

$$G(r) = 4\pi r \left[\rho(r) - \rho_0\right] = \frac{2}{\pi} \int_0^{Q_{max}} \left[S(Q) - 1\right] \sin Qr \, dQ$$

,where $\rho(r)$ and ρ_0 are the atomic number density and the average number density, respectively. And Q_{max} is the maximum scattering wave vector.

In the obtained data, the atomic pair distribution function (G(r)), describes the distribution of distances between pairs of particles contained within a given range. Figure 2.9 shows the schematics diagram of the concept of the paired distribution function [4]. It describes the distri-

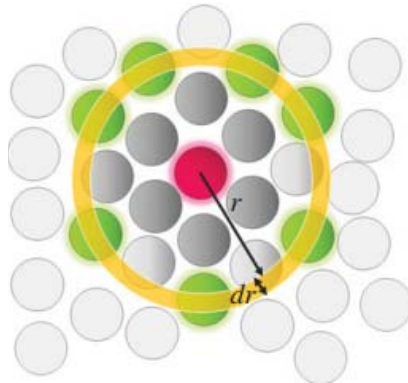

Figure 2.9: Schematics diagram of pair distribution function [4].

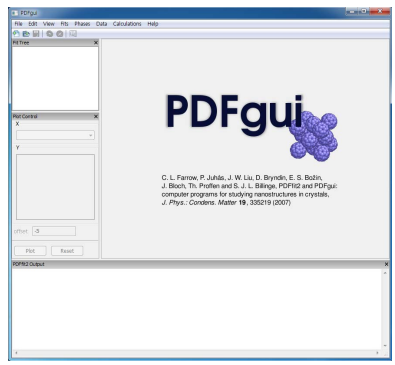

Figure 2.10: Screen-shot of starting page of PDFGUI [5].

bution of distances between pairs of particles contained within a given volume.

For a study of the local structure, a radial distribution function was calculated from the total scattering data and then analyzed using PDFGUI [5]. Figure 2.10 shows the screen-shot of the starting page of PDFGUI.

The first step when running PDFGUI is to input the initial values. As shown in figure 2.11(a), the initial structure of the lattice constant, the atom position and the thermal parameters analyzed from Rietveld refinement explained in 2.2.1 are used in input data. All atoms in a unit cell must be on the input list.

Figure 2.11: Introduction to PDFGUI. (a) Input initial values of structure and raw data. (b) Set refinement parameters and constraint. (c) Fit the data. (d) Fitted results are plotted.

After giving initial values for the structure with the raw data, the fitting parameters are set. The numbers subsequent are the fitting parameters here, as shown in Figure 2.11(b). The same numbers are the constrained parameters. The parameters of the raw data (e.g., Scale factor, Qdemp) can also be fitting parameters.

The fitting parameters are listed in the fitting tab. Fixing the parameters or not doing so during the matching process is controlled by a check box, as shown in Figure 2.11(c). The fitted results are shown in the output tab. These results can be checked by plotting the raw data, calculated data and the difference, as shown in figure 2.11(d).

By modulating the included pairs and fixing the fitted parameters, we can calculate the contribution of the pair distribution function of each atom pair. These results will be clarified in figure 6.9.

2.2.3 Magnetic structural analysis

When there are magnetic transitions, neutron diffraction can serve as a good technique for analyzing the magnetic structure. This will be the first step in understanding the magnetic properties of samples.

Figure 2.12 shows the basic process of a magnetic structure analysis. By comparing neutron diffraction data above and below the magnetic transition temperature, we can find the magnetic peaks such as those shown in figure 2.12(a). The propagation vectors, related to the size of magnetic unit cell, are then calculated using the peak positions. If the magnetic unit cell is identical to the crystal unit cell, the propagation vector is (0,0,0) as shown in figure 2.12(b). Based on the space group of the crystal system and the propagation vector, possible magnetic space groups can be calculated (figure 2.12(c)). By testing the magnetic structure candidates, the magnetic structure can be determined (2.12(d)).

We can calculate the magnetic structure with the method explained above. This method is used to determine the magnetic structures of $YMn_{1-x}(Al/Ga)_xO_3$ (section 5.3) and $PbFe_{0.5}Nb_{0.5}O_3$ (section 6.3).

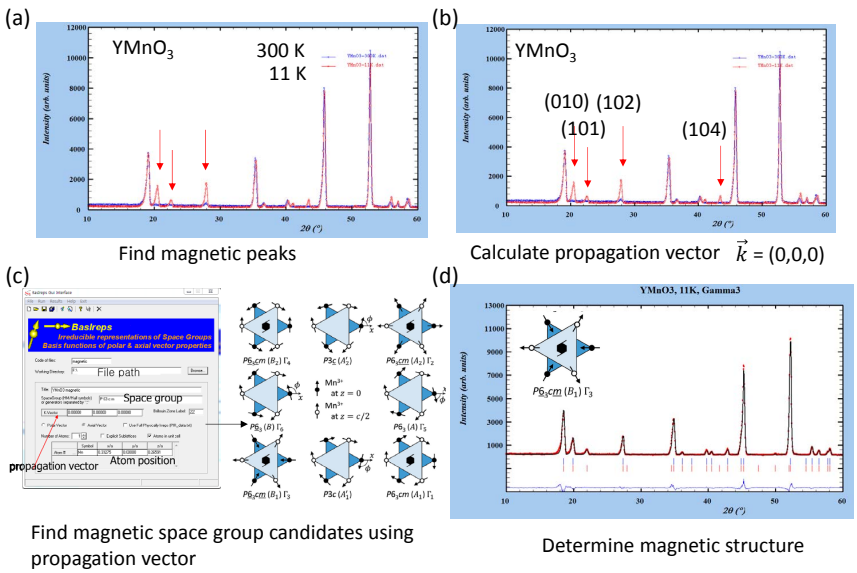

Figure 2.12: Process of magnetic structure analysis. (a) Find magnetic peaks. (b) Calculate propagation vector. (c) Find magnetic space group candidates using propagation vector. (d) Determine the magnetic structure

3. Studies on the high-temperature ferroelectric transition of multiferroic hexagonal manganite $RMnO_3$

Hexagonal manganite materials are multiferroic materials with two highly-dissimilar phase transitions: a ferroelectric transition (from $P6_3/mmc$ to $P6_3cm$) at a temperature higher than 1000 K and an antiferromagnetic transition at $T_N \sim 75$ K. Despite its critical relevance to the intriguing ferroelectric domain physics, the details of the ferroelectric transition are yet not well known to date primarily because of the ultra-high transition temperature. Using high-resolution and high-temperature X-ray diffraction experiments, we show that the ferroelectric transition is a single transition of weak first order and R-O_P displacement is the primary order parameter. This structural transition is then simultaneously accompanied by MnO_5 tilting and the subsequent development of polarization.

3.1 Two dimensional triangular lattice hexagonal manganite

Multiferroic materials have attracted considerable interest over the past decade or so. Since the initial call for search of then a new class of materials in early 2000s [6], we have witnessed a growing number of compounds joining the category of multiferroic systems. However, it is fair to say that among the numerous multiferroic compounds two materials stand out most. One is the rare room-temperature multiferroic $BiFeO_3$ and another is the hexagonal manganites. The hexagonal manganites do not offer as much potentials in applications as $BiFeO_3$. Nonetheless, they have been a constant source of new discoveries: a more recent case of point is the intriguing domain physics found in some of the hexagonal manganites that has been interpreted in terms of the Kibble-Zurek mechanism [7].

Hexagonal manganites (h-$RMnO_3$) with rare-earth elements of smaller

ionic size (R = In, Y, Ho - Lu) have both a ferroelectric transition (T_C >1000 K) and an antiferromagnetic transition (T_N ~75 K). During the ferroelectric transition from a high-temperature $P6_3/mmc$ structure to a low-temperature $P6_3cm$ structure, a macroscopic electric polarization is induced, reaching a value of 5.6 μ C/cm^2 at room temperature for h-$YMnO_3$ [8, 9]. Naturally, the structural aspect of both transitions has been the focus of intensive research [9, 10]. As compared to the perovskite structure with rare-earth elements of larger ionic size (R = La – Ho), the hexagonal $RMnO_3$ forms a unique structure with an ideal two-dimensional (2D) triangular lattice with MnO_5 polyhedron in the paraelectric phase of the $P6_3/mmc$ space group. At low temperatures, they undergo a magnetic ordering around 75 - 120 K with a so-called 120 degree noncollinear structure while the rare-earth moments go through their own ordering at much lower temperature, typically below 10 K. When the Mn moments order, it is accompanied by a large spin-lattice coupling [10]: which in turn appears to trigger a magnetoelectric coupling. More recently, it was shown that the noncollinear magnetic order provides an unusual magnon-phonon coupling, producing new magnetoelastic modes [11].

Figure 3.1(a) and(b) show the structures of h-$RMnO_3$ above and below the T_C. They have been well known since the 1970s [12]. During a transition, cells triple in the ab plane and polarization is induced along the c axis.

Although the space groups at both high and low temperatures have been rather well known since 1970s [12] as figure 3.1 show, the exact structural transition path between the two phases still remains unresolved. In principle, based on group-subgroup analysis, there can be 4 possible paths of structural transitions: they are the 3 modes of distortion for $P6_3/mmc$: Γ_2^- at q=(0,0,0), and K_1 and K_3 at k=(1/3,1/3,0). One additional mode is Γ_1^+ that is fully symmetric. Some paths allow an intermediate phase of different space groups while others directly go to the low-temperature $P6_3cm$ structure [13–15]. A complete understanding of the nature of the ferroelectric transition is extremely important, not least because the high-temperature structural transition induces the unusual trimerization of Mn^{3+} ions and subsequently generates the six ferroelec-

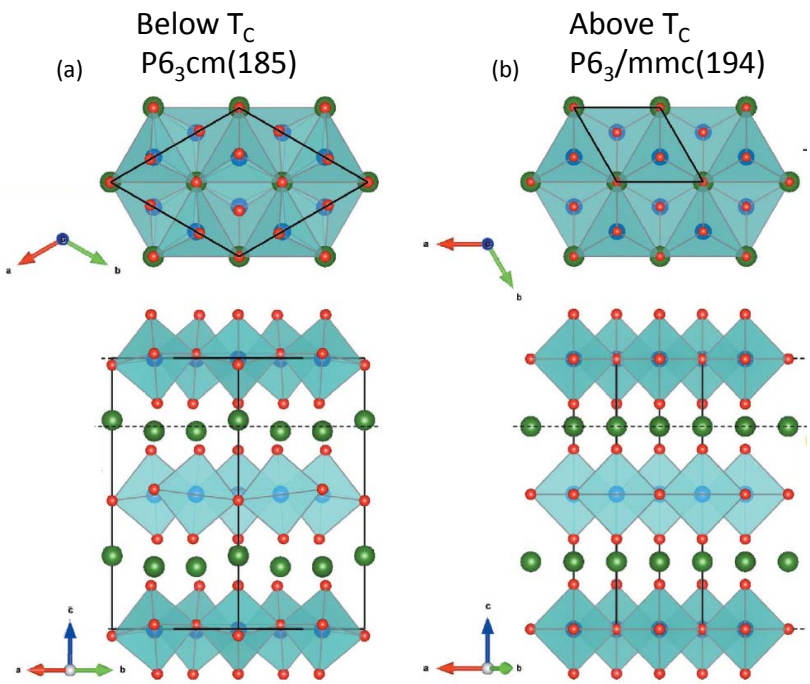

Figure 3.1: Structure for h-$RMnO_3$ (a) $P6_3cm$ and (b) $P6_3/mmc$

tric domains with intriguing vortex patterns: which itself has become the focus of intense recent studies [7, 16].

Among the two early theoretical works on the high-temperature transition, the first one was done by van Aken et al. [9]: using a first-principle density functional theory (DFT) and analyzing their X-ray diffraction data, they came to a conclusion that 'bulking of MnO_5 polyhedron accompanied by Y-O_P displacement' produces an energy minimum for the ferroelectric phase. About the same time, Fennie and Rabe carried out their first-principle calculations [17] independently. According to their calculations, only the K_3 mode is possible among the four paths with the K_3 mode inducing the Γ_2^- mode and producing the electric polarization [17].

Figure 3.2 shows the possible path tree between the $P6_3/mmc$ and the $P6_3cm$ structure. There are two possible different structural space groups, $P6_3/mcm$ and $P6_3mc$ between them. Identical structural intermediate phases such as $P6_3/mmc$ and $P6_3cm$ structures, indicating that an iso-symmetric transition are also possible.

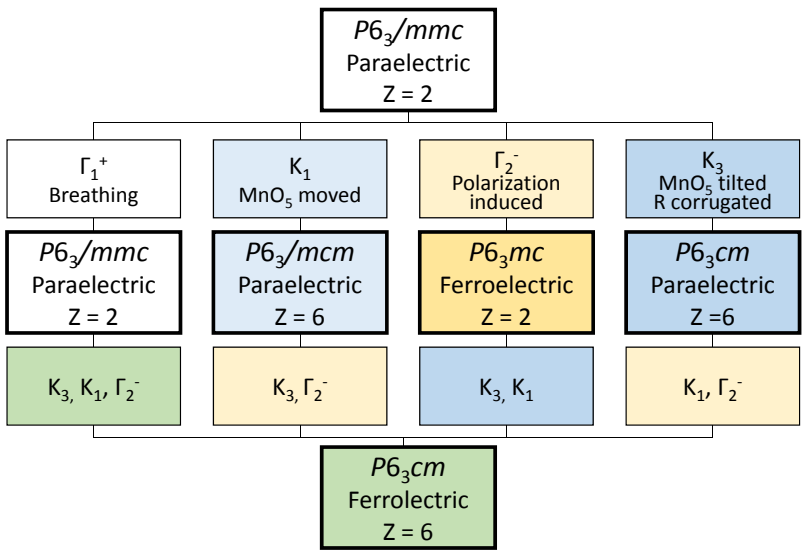

Figure 3.2: Group-subgroup relation tree

As regards the existence of the intermediate phase, there have been several conflicting experimental reports. For example, at least two papers claimed that h-$RMnO_3$ has a paraelectric $P6_3cm$ intermediate phase [15, 18]. The reported transition temperatures were around 1200-1450 K for the first structure transition and around 850-1100 K for the second phase transition [15, 18]. On the other hand, two other groups argued for a different intermediate phase of $P6_3/mcm$ [19, 20]. However, Jeong et al. claimed that there is no evidence for any intermediate phase based on their total scattering data [21]. Even for the $P6_3cm$ intermediate phase, there were two different reports about its ferroelectric nature: one is that the intermediate phase should be antiferroelectric [22] while there is also a report that the intermediate phase be ferroelectric [23].

A more recent report by Lilienblum et al. [24] suggests that the supposedly second transition to the putative intermediate phase is not a real phase transition, but rather caused by finite-size scaling effects. They measured the electric polarization by a second harmonic generation technique and calculated the MnO_5 tilting mode and the discreteness parameter. Their discreteness parameter can be understood as the movement of Mn atoms, which is basically the K_1 mode in our case. They argued that this discreteness parameter arising from the finite size

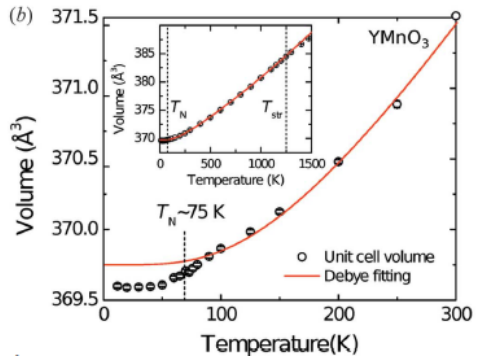

Figure 3.3: Unit cell volume curve of h-$YMnO_3$

effects makes the false claim of a second transition [24].

We measured the unit cell volume as a function of the temperature and attempted to determine the effects of a structural transition on the volume as shown in figure 3.3. There were no anomalies in the structural transition temperature, which means that the system shows second-order transition. If they are first order, they are weak.

In order to answer the question of the transient phase transition, we have undertaken careful high-resolution x-ray diffraction studies on all the hexagonal manganites. As compared to the previous studies, the key difference in our studies is that we identified the four principal Bragg peaks, whose temperature-dependent intensity would faithfully reflect the possible structural transitions associated with the four distortion modes. Using this approach, we are able to distinguish among the roles played by each mode regarding the ferroelectric transition. We discuss the implications of our data from the viewpoints of both experiment and theory.

3.2 Experimental details

Polycrystalline h-$RMnO_3$ samples with R = Y, Lu-Ho were prepared by a standard solid-state reaction method with stoichiometric R_2O_3 and Mn_2O_3 of reagent grade. Hydroscopic starting materials were pre-heated at 900 °C for 24 hours before weighing the mass and the final sintering

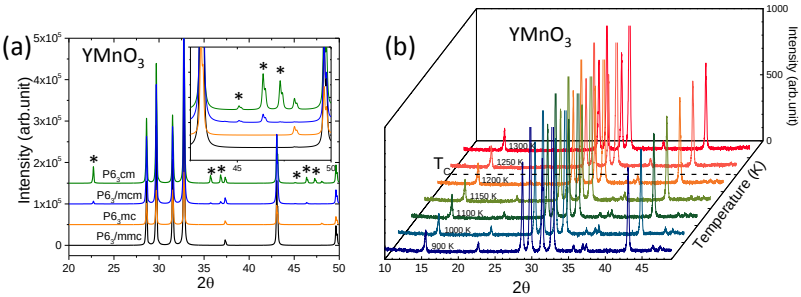

Figure 3.4: (a) Simulated X-ray diffraction results of h-$YMnO_3$ for four space groups: $P6_3/mmc$, $P6_3/mcm$, $P6_3mc$, and $P6_3cm$ structures with * marking the superlattice peaks. (b) Experimental data of h-$YMnO_3$ collected at seven representative temperatures below and above the transition temperature. The dashed line indicates the ferroelectric transition temperature.

was carried out at 1300 -1400 °C for 24 hours. Since $InMnO_3$ is harder to stabilize, an extra amount of Bi_2O_3, at a level of few weight %, was added before the final sintering. All our samples were checked by X-ray powder diffractometer (Bruker, D8 Advance), and found to form in the single phase of the $P6_3cm$ structure, except for h-$InMnO_3$. Even these samples contains a small amount of impurity, but its impurity peaks are well separated from the main peaks of hexagonal h-$InMnO_3$ so we can ignore it for our analysis.

We undertook high-temperature X-ray powder diffraction experiments to examine in detail the temperature dependence of several strong Bragg peaks from 700 to 1475 K with the high-resolution diffractometer (Bruker D8 Advance). All our measurements were carried out at every 25 K step with the counting time of 30 – 300 sec for every 0.02° step. For the (212) peak for h-$YMnO_3$, we reduced the temperature step further to 3 K over the temperature range between 1210 and 1260 K in order to obtain more data points with finer steps near the ferroelectric transition. Simulation and analysis were done by using FullProf [25].

3.3 Determination of structure transition path

One of the key issues was how to determine a possible intermediate phase as discussed in Refs. [19, 20]. As figure 3.2 shows, in principle, there are two possible space groups, $P6_3mc$ and $P6_3/mcm$, for the intermediate phase, which has a group-subgroup relation with the $P6_3/mmc$ and $P6_3cm$ space groups [14]. To illustrate the key differences in the diffraction patterns for each of the four space groups, we simulated the X-ray diffraction patterns in Fig. 3.4(a). Here one can immediately notice that careful diffraction studies can, in principle, distinguish each phase from one another. Since the room temperature structure of $P6_3cm$ has a larger unit cell than $P6_3/mmc$, there are several superlattice peaks if a direct transition should occur between the two end phases. On the other hand, if the intermediate phase is $P6_3mc$ with no Mn trimerization, there can be only an increase in the intensity of the (006) peak at 2θ=48°.

Based on the experimental data shown in Fig. 3.4(b), we can easily rule out both intermediate phases of either $P6_3mc$ or $P6_3/mcm$ as our data exhibit several superlattice peaks, notably the (212) peak, immediately below the transition temperature that cannot be explained by either of the two phases. Further close examination of the overall diffraction patterns and its careful comparison with those simulation results reveals that the ferroelectric transition is a direct transition from the high-temperature $P6_3/mmc$ to the room temperature $P6_3cm$: i.e. no intermediate phase with a different space group.

3.4 Separation of atomic movements

Figure 3.5 shows the basic concept of a mode separation. It is assumed here that there are two particles which can only move up and down. When the particles are moved, the movements can be separated into two types, those in the antifferoic mode and ferroic mode. Each mode is a symmetry breaking of the inversion and the mirror. A similar analysis can be applied to our system. Atom displacement during a transition can be separated into different modes based on the symmetry.

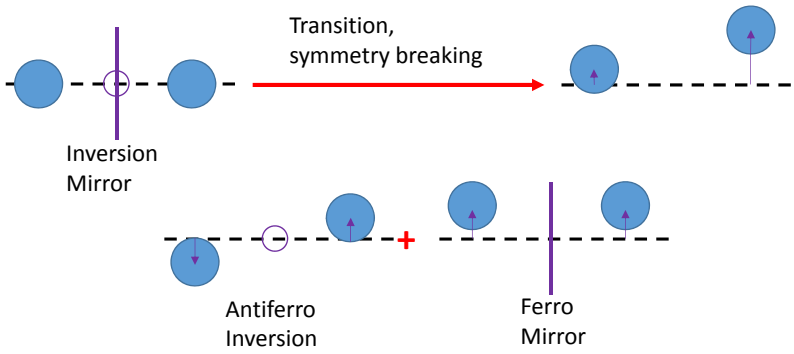

Figure 3.5: Toy model for mode analysis

Hexagonal manganites undergo a structural transition from the high-temperature $P6_3/mmc$ structure to the low-temperature $P6_3cm$ structure with the four possible modes: Γ_1^+, Γ_2^-, K_1 and K_3 [26]. Fig. 3.6 illustrates the detailed movement of atoms for each mode. For example, the K_3 mode shown in Fig. 3.6(a) includes the MnO_5 tilting and the corrugation of rare-earth elements [14, 15]. The MnO_5 tilting includes the movements of the apical oxygen atoms (O_A) along the ab direction, which would rotate the MnO_5 polyhedron. On the other hand, the corrugation of rare-earth elements includes the movement of rare-earth elements and the planar oxygen atoms (O_P) along the c axis. Importantly, the apparently complex displacements involving the K_3 mode are antiferroelectric in nature. Fig. 3.6(b) also shows the Γ_1^+ breathing mode, in which O_P atoms move antiferroelectrically and distort the MnO_5 polyhedron. For comparison, the K_1 mode shown in Fig. 3.6(c) involves MnO_5 movements and the Mn trimerization. In this case, the planar oxygen atoms (O_P) and Mn atoms move on the ab plane, which also distorts the MnO_5 polyhedron. And then there is the only polar mode of Γ_2^- in Fig. 3.6(d). This Γ_2^- mode shifts all the rare-earth elements together along the c-axis whereas the planar oxygen atoms (O_P) move in the opposite direction, producing the net electric polarization along the c-axis. We note that the apical oxygen (O_A) atoms move in the same direction as the rare-earth elements and reduce the size of the total electric polarization.

As mentioned, there are altogether four possible space groups for the ferroelectric transition: $P6_3mc$, $P6_3/mcm$, $P6_3/mmc$, and $P6_3cm$ [14, 19,

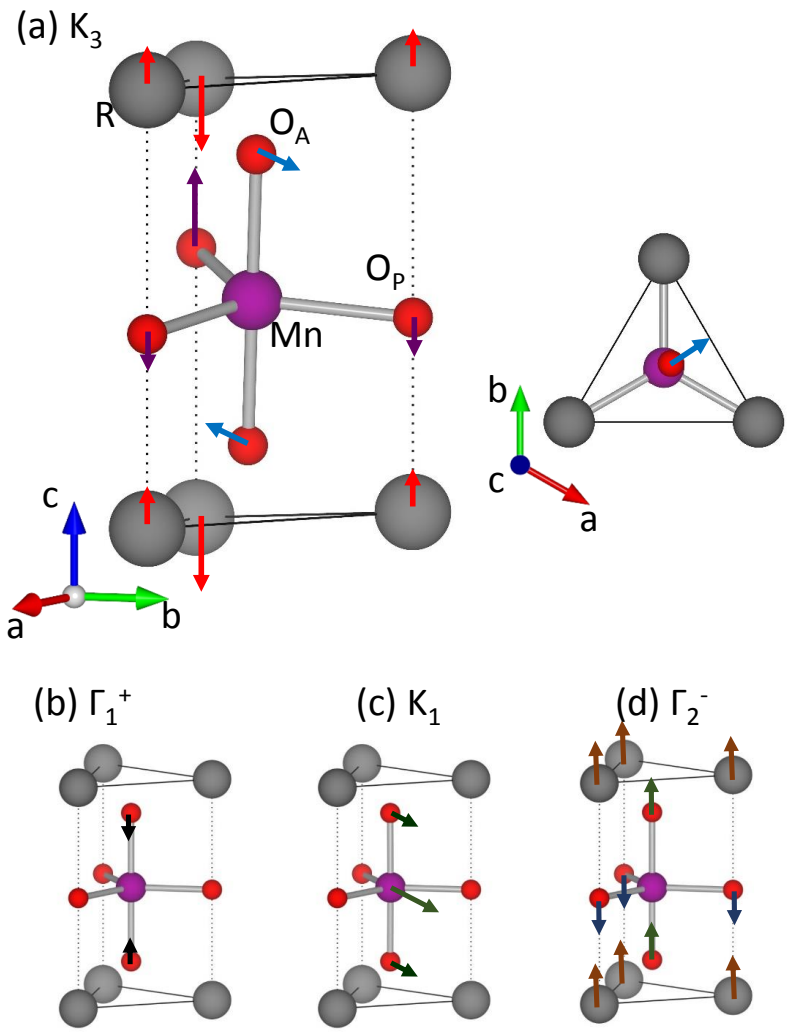

Figure 3.6: Direction and relative size of atomic displacements of h-$RMnO_3$ for the four possible modes. (a) K_3, (b) Γ_1^+, (c) K_1 and (d) Γ_2^-. The arrows in the figure indicate the direction of the atomic displacement when the corresponding mode is active, and the length of the arrows is chosen to be proportional to the magnitude of the atomic displacements.

20]. We can easily rule out both intermediate phases of either $P6_3mc$ or $P6_3/mcm$ as our data exhibit several superlattice peaks. That is, the ferroelectric transition is a direct transition from the high-temperature $P6_3/mmc$ to the room temperature $P6_3cm$. A possible $P6_3/mcm$ phase will produce several superlattice peaks related to the K_1 mode, which then rules out the K_1 mode as the primary order parameter.

As we have already ruled out the K_1-driven $P6_3/mcm$ as an intermediate phase, we can focus on the two other possibilities: Γ_2^- and K_3, for our subsequent discussion. Since each atom move independently and they are in irreducible representation, we can think of separating them to trace each movements as a function of temperature. Of great importance, we can further separate the K_3 mode into two distinct structural motions: the R-O_P displacement along the c-direction and the MnO_5 tilting. True, these two modes are interconnected for the actual transition in real materials. However, by dividing the modes up into the two different parts of the structural change, we will be able to better understand which one of the two structural changes of the K_3 mode is more important, i.e. as the primary order parameter, as we will demonstrate later in the discussion.

For further discussion, several theoretical diffraction patterns are simulated in Fig. 3.7 for the three different cases of distortion together with the two space groups of $P6_3/mmc$ (thick line) and $P6_3cm$ (dash-dot line). To make our discussion simple and transparent, we have assumed in our simulation that one of the two distortions of the K_3 mode can be switched off individually. For example, we kept the MnO_5 tilting off in our simulation (thin line) for the only R-O_P displacement distortion of the K_3 mode: this R-O_P displacement involves the z-position movement of R and O_P atoms (see also Fig. 3.6). For this R-O_P displacement the two sites of the rare-earth atoms move in the opposite directions with a ratio of 2:1, which would accidentally cancel out the total induced dipole moment. Our simulation for the MnO_5 tilting (dashed line) requires the ab-plane movement of O_A atoms in the K_3 mode. Finally, we also show our simulation results for the Γ_2^- mode (dash-dot-dot line). For this case, R and both oxygen (O_P and O_A) move in the same direction and induce the total polarization along the c-axis, i.e. becoming the only polar mode.

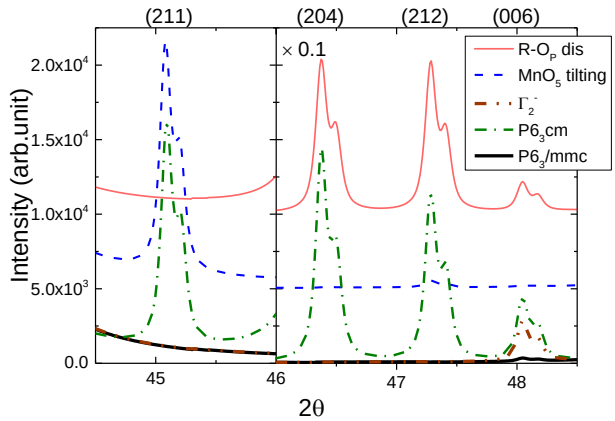

Figure 3.7: Simulated X-ray diffraction results for $YMnO_3$. Blown up picture of the simulation results with three specific distortions: R-O_P displacement (thin line), MnO_5 tilting (dashed line), both of the K_3 mode, and the Γ_2^- mode (dash-dot-dot line). For comparison, we also calculate the diffraction patterns for the high-temperature $P6_3/mmc$ (thick line) and the low-temperature $P6_3cm$ structure (dash-dot line). (HKL) lists are based on the $P6_3cm$ structure.

An interesting pattern already emerges in our simulation results shown in Fig. 3.7 that the Bragg (211) peak is mostly due to the MnO_5 tilting: we estimate around 90% of the total intensity comes from the MnO_5 tilting distortion. For comparison, a similar percentage of the (212) and (204) peaks results from the R-O_P displacement. This observation allows us to separate the relative contribution of the two distortions of the K_3 mode and, more importantly, to follow up the temperature dependence of each distortion individually. For the Γ_2^- mode, we found that the (006) peak appears to follow the ferroelectric structural transition and the development of the polarization. As it becomes clear now, this possibility of being able to examine the individual distortions independently is a great advantage of our approach in this work as compared with the full Rietveld refinement analysis done in many previous reports.

With this information, we are now ready to look at the data. We show the raw data in Fig. 3.8 for both h-$YMnO_3$ and h-$ErMnO_3$. As can be seen in the contour plots, all the Bragg peaks, mostly the (204) and (212) peaks, show a clear change at the reported ferroelectric transition temperature (white line). In the case of the (211) peak, it is relatively

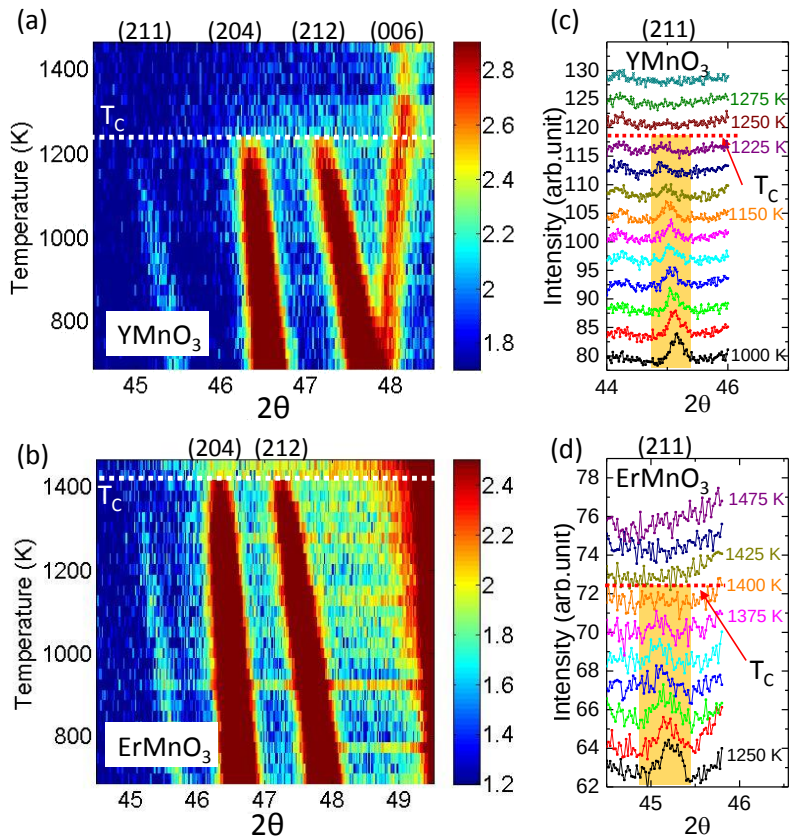

Figure 3.8: Temperature-dependent X-ray diffraction data. Contour plot of temperature-dependent X-ray diffraction data for (a) h-$YMnO_3$ and (b) h-$ErMnO_3$ with the transition marked by white horizontal lines. Blown-up pictures of the (211) peak are shown for (c) h-$YMnO_3$ and (d) h-$ErMnO_3$ with longer counting time.

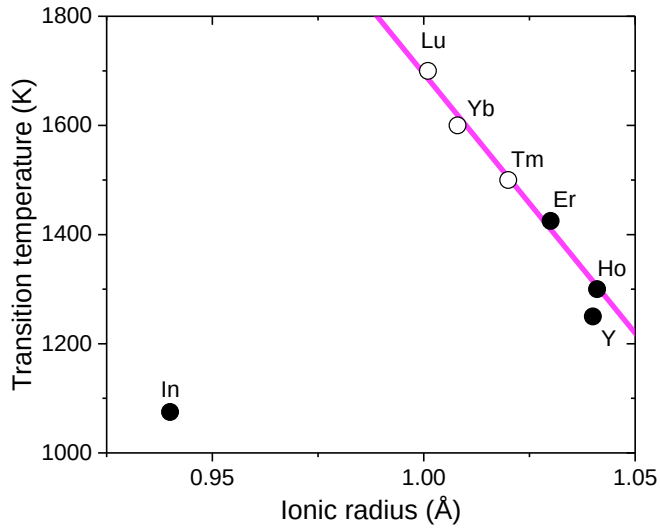

Figure 3.9: Ionic size dependence of the transition temperature with open circle for the data points taken from Ref. [27].

weak and so harder to follow as it gets closer to the transition temperature. For this reason, we have made two separate plots of the (211) peaks for both samples in Figs. 3.8(c) and 3.8(d). In the blown-up pictures, the (211) peak disappears clearly above the transition temperature for both systems. On the other hand, the (006) peak of h-$YMnO_3$ shows a much slower temperature dependence as we will discuss later. For h-$ErMnO_3$ the (006) peak is located very close to the (212) peak and it is rather difficult to separate it from the other peaks. Nonetheless, our data show that all the superlattice peaks disappear at the same temperature, indicative of a single transition: which is different from some of the previous reports [22, 23].

We show the ionic size dependence of the ferroelectric transition in Fig. 3.9. As h-$RMnO_3$ with R = Tm, Yb and Lu have their ferroelectric transition temperature above the maximum temperature of our systems, we took the data point (open circle) from Ref. [27]: the filled symbols are from our experiments reported here. As one can see, with the ionic size decreasing from Lu to Y the transition temperature gets linearly reduced. The only exception is h-$InMnO_3$ that shows the lowest transition temperature among all h-$RMnO_3$ although In has the smallest ionic radius. At

this moment, we do not know what the main origin of this deviation is in the transition temperature for h-$InMnO_3$.

We would now like to examine the temperature dependence of the four Bragg peaks in further detail. For this, we fitted each of the peaks using a pseudo-Voigt function with a fixed ratio (35% Gaussian and 65% Lorentzian) and a fixed wavelength ratio (Cu $k_\alpha 1$: Cu $k_\alpha 2$ = 2:1). We have taken great care in subtracting background to have the correct estimate of intensity. We plot the estimated area of the peaks as a function of temperature for h-$YMnO_3$ and h-$ErMnO_3$ in Fig. 3.10 and 3.11. This plot makes an immediately noticeable point about the temperature dependence: the (204) and (212) peaks change rather abruptly at the transition temperature while the (211) and (006) peaks are very gradual across the transition temperature.

3.5 Temperature dependence of atomic movements

This abrupt behavior of the (204) and (212) peaks can be taken as evidence that the phase transition may be a weak 1st order. The lines underneath the two peaks in our Figs. 3.10(a) and 3.10(b) are our theoretical calculations using the Ginzburg-Landau analysis for a 1st order transition (solid line): F=$\frac{\alpha_2}{2}Q^2 + \frac{\alpha_4}{4}Q^4 + \frac{\alpha_6}{6}Q^6$, where F is the Ginzburg-Landau free energy and Q is the displacement amplitude with α_2 = a(T_C-T) and T_C being a critical temperature [28]: the dashed line in Fig. 3.10a is for what is expected of a 2nd order transition. We used T_C values of 1236 and 1421 K for h-$YMnO_3$ and h-$ErMnO_3$, respectively. Interestingly, the 3D XY model used in Ref. [16] fails to fit the temperature dependence too (dashed-dot line in Fig. 3.10a). For comparison, the temperature dependence of both (211) and (006) peaks can be explained by Ginzburg-Landau analysis for a 2nd order transition in Fig. 3.10(b). We also plotted the usual Debye-Waller (D-W) factor in Fig. 3.10(b). A similar plot is made for h-$ErMnO_3$ in Fig. 3.11.

Here we would like to comment that our observation of the abrupt or weak 1st order phase transition appears not to be consistent with the estimated coefficients of the zero-temperature energy surface in the previous DFT calculations [9, 17]. However, given how high the transition

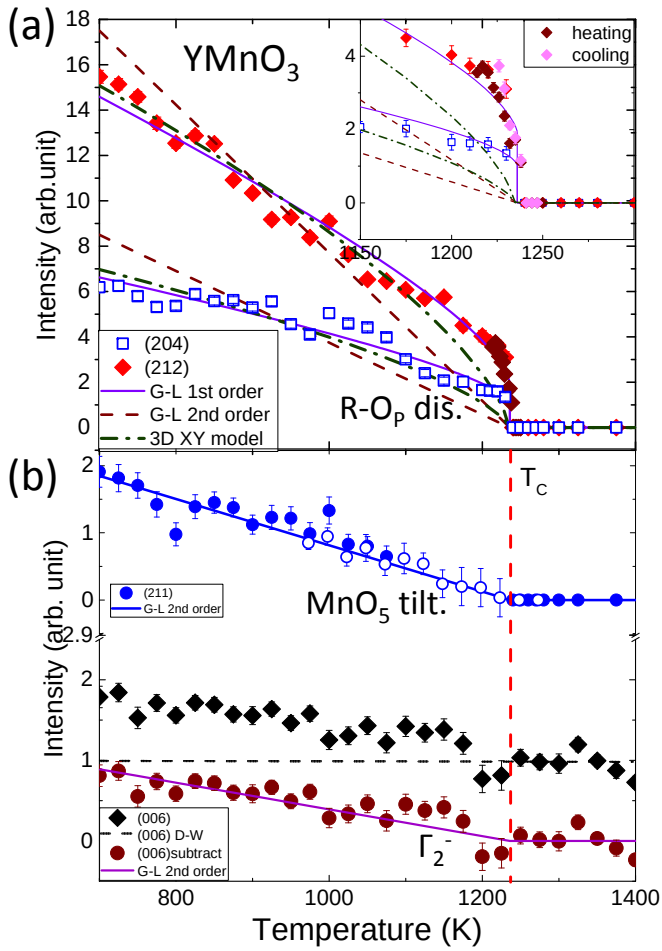

Figure 3.10: Temperature dependence of the peak intensity of the four Bragg peaks. (211), (204), (212) and (006) for h-$YMnO_3$ (see the text). (a) Data points were collected with much longer counting time near the transition with warming and cooling. Solid (dashed) lines in (a) show the 1st (2nd) order G-L fitting results: for comparison, a line (dashed-dot) is also added for the 3D XY model used in Ref. [16]. Inset shows the blown-up picture of the data points and the fitting results near the transition temperature. (b) Circles (closed and open) represent data points of the (211) peak with the open symbols collected with longer counting time. We also made similar plots for the (006) peaks before (diamond) and after (circle) correcting for the usual temperature dependence of the Debye-Waller factor (dashed line).

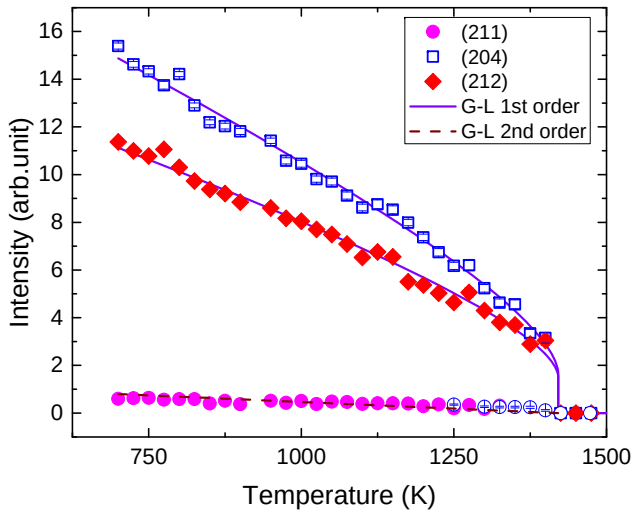

Figure 3.11: A similar plot as figure 3.10 is made for h-$ErMnO_3$.

temperature is, it is not unreasonable to assume that the coefficients extracted from the zero-temperature DFT calculations get renormalized and the sign of α_4 can change at higher temperature as our analysis indicates.

If we combine both the experimental data shown in Fig. 3.10 and the simulation result in Fig. 3.7, the following picture emerges of the ferroelectric transition. The R-O_P displacement of the K_3 mode that is responsible for the (204) and (212) peaks undergoes a probably weak 1st order phase transition, and so becomes the primary order parameter of the ferroelectric transition. Simultaneously the MnO_5 tilting of the K_3 mode that is responsible for the (211) peak gets stabilized subsequently and becomes a secondary order parameter. On the other hand, there is a very gradual increase in the intensity of the (006) peak that arises from the polar Γ_2^- mode on top of the usual Debye-Waller factor in Fig. 3.10. Within the uncertainty of our experiment, we conclude that the polarization, i.e. the (006) peak, starts to develop right below the structural transition. To demonstrate this point further, we subtracted the theoretical temperature dependence of the Debye-Waller factor from the measured intensity of the (006) peak and show the difference in the Fig. 3.10(b). This is also consistent with the experimentally measured

polarization by the SHG technique in Ref. [24].

We would now like to compare our main conclusion with those of previous reports. First, van Aken et al. discussed the relationship between the Mn-O polyhedral buckling and the Y-O_P displacement [9]. In their paper, they argued that the Mn-O polyhedral buckling is a primary order parameter, and the ferroelectric displacements of Y-O_P and the buckling (or tilting) of Mn-O bonds are energetically favored with respect to the centrosymmetric structure. On the other hand, Fennie et al. studied the relationship between the K_3 and Γ_2^- modes and concluded that the K_3 phonons are strongly unstable and easily coupled to the Γ_2^- mode [17]. They argued that the Y-O_P displacement is a primary mode while the Γ_2^- mode is secondary, in good agreement with our results.

However, there is also discrepancy between our results and some of the previous reports. First, in our results only the Y-O_P displacement mode shows an abrupt change at the transition temperature while the MnO_5 tilting shows a much slower continuous temperature dependence. This observation seems to differ from what is reported, for example in the latest paper by Lilienblum et al. [24], where the MnO_5 tilting was claimed to have a much faster temperature dependence right below the structure transition. Then, there are several reports that the ferroelectric transition temperature is lower than the actual structure transition [13, 15, 29]. Unlike these reports, the temperature dependence of the (006) peak show that the actual polarization also starts right at the structural transition. We note that our conclusion on this point is consistent with those in Ref. [24]. Moreover, we would like to note that with the improper coupling of a PQ^3 type the phase transition of P, i.e. the intensity of (006), should be of 1st order. However, as discussed by Fennie and Rabe [17], the PQ^3 coupling tends to suppress P close to the transition (while P $\propto$ Q for large values of Q).

Finally, we note that our conclusion is similar to that of Ref. [23] in that there is no intermediate phase with space group $P6_3/mcm$. However, there is also discrepancy, namely the evidence of the second transition. In our data, we failed to observe any evidence for this second transition: this second transition was rather weak even in Ref. [23]. It is also worth noting that their analysis of mode-decomposition using AMPLIMODES

reveal that all four modes seem to undergo rather abrupt change at the ferroelectric transition. What we have shown in this paper is that by measuring and examining the Bragg peaks associated with the four modes we can clearly follow the temperature dependence of each mode directly from the measured data and reach a conclusion on the different temperature dependence of the modes.

3.6 Summary

To summarize, we can make the following conclusions based on the experimental data and the theoretical simulation. First, there is only a single transition of weak first order nature from the high-temperature $P6_3/mmc$ structure to the low-temperature $P6_3cm$ structure with no intermediate phase. By examining the individual distortions independently, we also found that this transition is mainly driven by the $R-O_P$ displacement, which is then accompanied by the MnO_5 tilting mode and the polarization mode that vary more slowly. Therefore, we conclude that the R-O_P displacement of the K_3 mode is the primary order parameter of the high-temperature structural transition.

4. Geometrically frustrated ferroelectric transition and alloying effects of multiferroic Y(Mn,Al/Ga)O_3

Multiferroic hexagonal manganites $RMnO_3$ have a very high ferroelectric transition temperature around and above 1200 K depending on the rare-earth elements, and a reasonably large electric polarization of 5.5 μ C/cm^2 at room temperature. We confirmed that the ferroelectric transition is driven by the combination of R-O_P displacement and MnO_5 tilting under possibly geometrical frustration due to the triangular lattice of MnO_5 network in previous chapter. In order to better understand the question of the geometrical frustration of the ferroelectric transition, we studied the alloying effects using two elements with the same valence but a different ionic size: Al and Ga on the Mn site of h-$YMnO_3$. Through detailed structural studies and atomic-probe measurements of KPFM (Kelvin probe force microscopy) and PFM (Piezoresponse force microscopy), we conclude that there is drastic alloying effect with Al, whose ionic size is much smaller than Mn. It is in stark contrast with our observation that Ga having a similar ionic size with Mn does not change the ferroelectric transition up to 50% alloying. This drastic difference in the alloying effect of Al and Ga is a clear evidence of the geometrical frustration of the ferroelectric transition of h-$RMnO_3$.

4.1 Two dimensional triangular lattice hexagonal manganite

Hexagonal manganite is one of the popular multiferroic materials with ferroelectric transition around T_C = 1200 K and antiferromagnetic transition around T_N = 70 K [13]. When the hexagonal manganite $RMnO_3$ undergo a structure transition from paraelectric $P6_3/mmc$ to ferroelectric $P6_3cm$ structure, it is rather abrupt, close to a weak first order transition with no intermediate phase (chapter 3). In principle, altogether four separate modes: Γ_1^+, Γ_2^-, K_1 and K_3, are induced during the transition [15].

Among the four modes, the K_3 mode is a primary order parameter, which itself can be separated into two components: R-O_P displacement mode and MnO_5 tilting mode. According to our latest high-temperature structure studies, the R-O_P displacement appears to be driving the phase transition with almost first order character. This R-O_P displacement is then accompanied by MnO_5 tilting and Γ_2^- polarization mode (chapter 3). Although we have now a generally good understanding of the ferroelectric transition of hexagonal $RMnO_3$, nonetheless the geometrical frustration due to the Mn triangular lattice remains less well explored. For this, we think that doping experiment can be a convenient way of learning this part of physics.

There were a few doping studies on the hexagonal manganites. However, they were mostly concentrated on the magnetism side. For example, it was found that with increasing doping concentration on the Mn site the signatures of the antiferromagnetic ordering gets subdued. On the other hand, doping at the R site seems to have much weaker effects: the antiferromagnetic transition seems to remain unchanged across the whole doping range of h-(Y,Lu)MnO_3 [30]. Although there is not much of experimental works on the doping effects on the ferroelectric transition, a theoretical study found that Ga doping on h-$InMnO_3$ induces a change in the space group as doping ratio gets increased [31]. Given the lack of experimental studies on the doping effects on the ferroelectric transition and especially the question of geometrical frustration of the triangular lattice, it is certainly an interesting question how the ferroelectric transition responds to controlled perturbation via doping at the Mn site. It will be especially useful if one can follow the detailed-temperature and doping dependence of those key distortion modes found in undoped system.

In this paper, we report the extensive studies of Al and Ga doping at the Mn site. As Al (67.5 pm) and Ga (76 pm) have different ionic radius: Ga have a very similar ionic radius to Mn (78.5 pm), we aimed to explore how the variation in the ionic size affect the ferroelectric transition. In doing so, we also hope that it will reveal hitherto unexplored geometrical frustration effects on the ferroelectric transition. One note of caution, as both Al and Ga have the same valence with Mn it is appropriate for

us to use alloying instead of doping. Thus we are going to use alloying hereafter. To examine the high-temperature structural changes, we employed both powder and single crystal XRD diffractometers. In addition, we used Kelvin probe force microscopy (KPFM) and Piezoresponse force microscopy (PFM) to probe the ferroelectricity directly. In this study, we found that as Al doping ratio increase, the ferroelectricity are rapidly suppressed and transition temperature decrease. In contrast, surprisingly there is very little doping effects when we used Ga up to 50%. We discuss these results in terms of geometrical frustration of the ferroelectric transition.

4.2 Experimental details

We prepared polycrystalline $YMn_{1-x}(Al/Ga)_xO_3$ using Y_2O_3, Mn_2O_3 and Al_2O_3/Ga_2O_3 by a standard solid state reaction method. All the starting materials prepared in stoichiometric ratio were mixed, pelletized, and sintered for several times. The final sintering condition was set to 1300°C for 24 hr. Single crystals were subsequently grown with the 4mm diameter feed rod of correct compositions by a floating zone furnace (Crystal Systems, Japan) under ambient conditions and the growth speed was 2mm/hr as explained in section 2.1.2. We note that the usual solid state reaction method can only manage to do 10% doping [32], while our single crystal growth can produce samples with much higher doping: 50% of Ga doping case. All our samples were checked to form in the single phase by powder XRD measurements.

We performed high-temperature powder X-ray diffraction experiments from 300 to 1473 K using a commercial diffractometer (D8 Advance, Bruker) after grinding the grown single crystals into fine powder. We also carried out single crystal X-ray diffraction using high-resolution single-crystal X-ray diffractometer (XtaLAB P200, Rigaku) from 300 to 1073 K using a gas flow type heater. We refined our data using FullProf [25].

Afterwards, we made PFM and KPFM measurements using an atomic force microscope system (Asylum Cypher, Oxford Instruments). Pt/Ir-coated Si cantilever (NCH/Pt, resonance frequency: 350 kHz, Nanoworld)

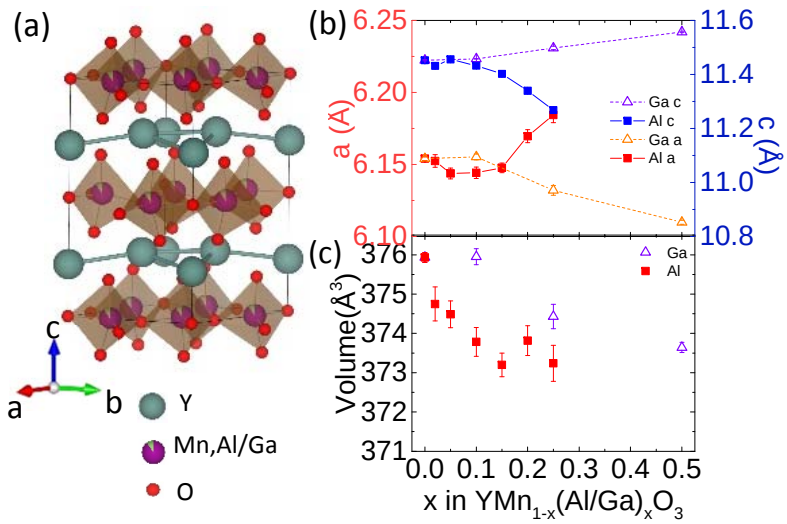

Figure 4.1: (a) Structure of h-YMn$_{1-x}$(Al/Ga)$_x$O$_3$. (b) Lattice constant depends on doping ratio. Lattice constant show systematic change. (c) Volume of unit cell depends on doping ratio. Volume get suppressed as doping ratio increase.

were used for both PFM and KPFM measurements. PFM images were acquired by applying an AC modulation voltage of amplitude of 10 V and a frequency of 350 KHz to the tip before and after applied biases over a square-shaped region of 1 μm $\times$ 1 μm (-10 V) and 3 μm $\times$ 3 μm(+10 V). The KPFM images were obtained using a lift mode with a drive frequency of 350 kHz and an AC modulation voltage of amplitude 1 V. The system captures the topography and the system then retraces that topography on the same line in order to keep a constant distance from the sample surface, 30 nm. Prior to the SPM experiments, the samples were heated to 150°C for 30 min to remove water molecules that had been adsorbed on the surface.

4.3 Results and analysis

Hex-YMnO$_3$ has $P6_3cm$ structure at room temperature, which forms with 2d triangular Y layer and another Mn 2d triangular layer with MnO$_5$ polyhedral. According to our XRD results, all our samples form in the

same space group $P6_3cm$ regardless of Al or Ga doping concentration. Figure 4.1(a) shows the crystal structure of h-$YMn_{1-x}(Al/Ga)_xO_3$: with Al and Ga doped at the Mn site it gets randomly mixed. Figure 4.1(b) and (c) show the lattice constants and volume as a function of Al and Ga doping, measured by single crystal XRD. As one can see, there is a gradual change in the lattice constant as doping ratio increase although Al and Ga doping have an opposite effect. While Al doping increase the a-lattice constant decrease the c-lattice constant, Ga doping produces the exactly opposite effects. But the overall effect on the unit cell volume is the same as both Al and Ga have smaller ionic size than Mn: ionic volume is Mn^{3+}(78.5 pm) >Ga^{3+}(76 pm) > Al^{3+}(67.5 pm). Thus, it is interesting how Ga and Al having smaller ionic size have such completely opposite effects on the a- and c-lattice constants. As we will argue later in the discussion, we think it is directly related to the doping dependence on Y-O hybridization, first, and ultimately the ferroelectric transition.

In order to study the doping dependence on the ferroelectric transition, we undertook the diffraction data at room temperature. Figure 4.2 shows the powder XRD data for all Al and Ga doping, which confirmed that there are no other impurity peaks for all the samples. It is well known that $YMnO_3$ undergoes a structure and ferroelectric transition from the $P6_3/mmc$ structure to the $P6_3cm$ structure at 1250 K. At this ferroelectric transition, there appears several superlattice peaks. Among the superlattice peaks, we marked a few stronger peaks in Figure 4.2(a) and (c): they are (102), (104), (204), and (212) peaks. We also plotted the (212) peaks as separate figures to further highlight the doping dependence on its intensity. As it is clear in the figures, the superlattice peaks get suppressed progressively with Al doping and they seem to disappear for higher than 15% of Al doping. In contrast, the same superlattice peaks remain unchanged even up to 50% of Ga doping. This strikingly different doping dependence on the superlattice peaks indicates that both Al and Ga with smaller ionic size produce completely different effects on the ferroelectric transition.

We performed structural analysis on h-$YMn_{1-x}(Al/Ga)_xO_3$ using single crystal XRD. Figure 4.3(b) shows the Y atom position from refinement at room temperature as a function of doping. As one can see, with

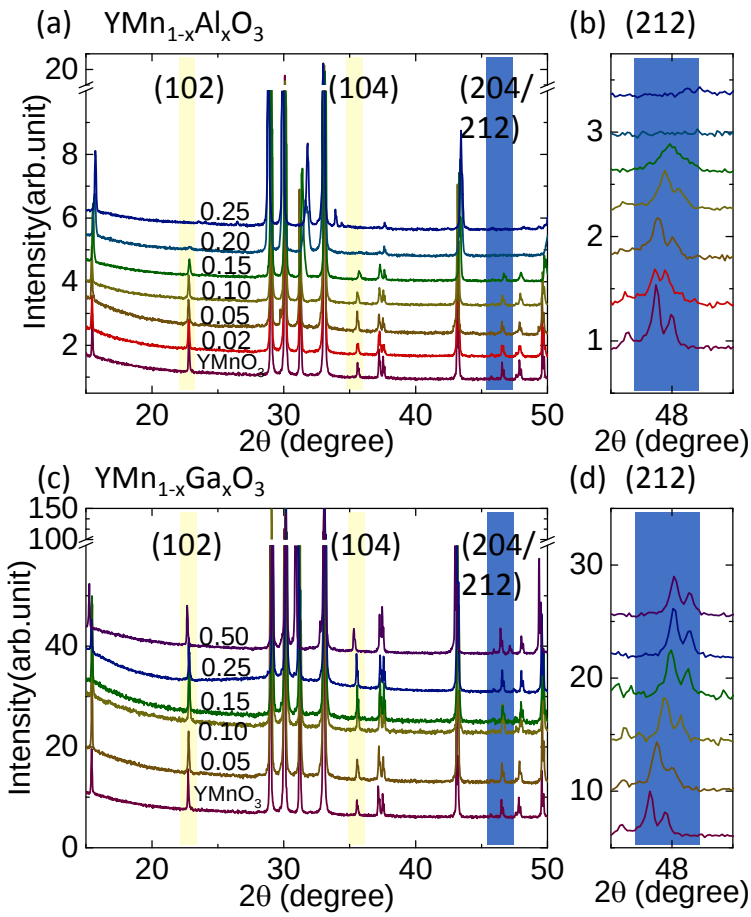

Figure 4.2: Powder XRD results of (a) h-$YMn_{1-x}Al_xO_3$ and (c) $YMn_{1-x}Ga_xO_3$. Highlighted region are peaks that are related to structural transition. (b) and (d) are (212) peaks. As Al doping rate increase, peaks' intensity are suppressed.

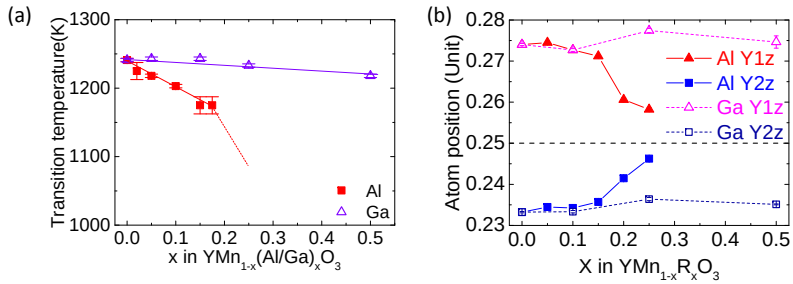

Figure 4.3: (a) Ferroelectric transition temperature depending Al/Ga doping ratio. Al doping reduce transition temperature a lot, while Ga doping do not change much. (b) Refinement results of Yttrium z position from XRD data

Al doping the Y position converges to the value of 0.25, indicating that it becomes paraelectric but remain as $P6_3cm$ structure. On the other hand, the Y position remains almost unchanged with Ga doping, again supporting our conclusion that Ga doped samples remains ferroelectric transition as strong as undoped sample.

Peaks related to structure disappear at the structural transition temperature, implying that the structural transition temperature can be determined by finding these peaks. Becasue the intensity of these peaks is decreased with an increase in the temperature, only using powder XRD is not enough for highly Al-doped samples, in which these peaks are quite small even at room temperature. Single crystal XRD is capable of finding weak signals that can be easily negligible. Highly doped Al samples show small structure related peaks, therefore single crystal XRD experiment is needed. We obtained a full transition temperature phase diagram using two machines, single crystal XRD and powder XRD results, the results of which are shown in figure 4.3. The transition temperature was greatly reduced when the Al doping ratio was increased, whereas it remained nearly identical when the Ga doping ratio was increased. Doping with Al induces many more changes than doping with Ga.

In order to check this doping dependence on the ferroelectric transition, we have carried out high-temperature diffraction studies on the focused region with some representative data shown in Fig 4.4. As sum-

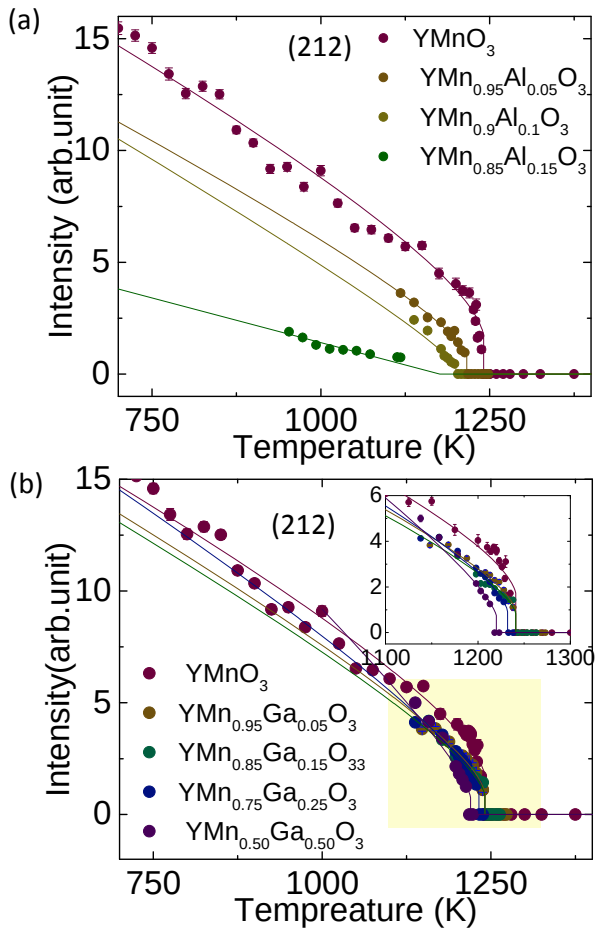

Figure 4.4: peaks explain R-O_P displacement mode. (a) Doping Al change transition behavior as second order while (b) Ga doping remains same. Solid line show Ginzburg-Landau analysis for a first order transition.

marized in the temperature dependence of the (212) peak, there are noticeable difference in the doping effects. First, with Al doping the transition temperature is reduced quite significantly from 1250 K for undoped sample to 1175 K for 15% of Al doping. Second, the transition that is originally a sharp transition of almost 1st order for undoped sample become a very smooth transition for 15% doping, indicative of 2nd order transition. The lines underneath the data points are our fitting results using Ginzburg-Landau free energy with a weak 1st order for undoped, 5, 10% doping and a 2nd order for 15% doping. In a complete contrast, there is a little noticeable effect on the overall temperature dependence for all the Ga-doped sample. There is neither change in the transition temperature nor the nature of the transition. All the line drawn for Ga-doped samples are for a weak 1st order. To make this point clearer, we show an enlarged picture of the data near the transition temperature as an inset. In Fig. 4.3, we summarize the doping dependence of Tc. We note that since the intensity of the superlattice peaks gets decreased significantly as increasing temperature, especially near the transition temperature, we used both powder and single-crystal XRD machines to plot the data points in Fig. 4.3.

To further confirm the ferroelectric property of doped $YMnO_3$, we compared the piezo response and surface potential pre and post the application of a bias through PFM and KPFM experiments. We note that all our PFM and KPFM measurements were done at room temperature. Figure 4.5. (a)-(d) show the results for $YMnO_3$, $YMn_{0.9}Al_{0.1}O_3$ and $YMn_{0.75}Ga_{0.25}O_3$ results. The undoped sample shows distinct intrinsic ferroelectric domains while doped samples present the blurred shapes or no domains on the area before polarization switching in Fig. 4.5 (b) and (c). On the other hand, 10-15% Al doped samples show the highest polarization switching rate among all the samples, which is also confirmed by KPFM results shown in fig. 4.5 (d) and (e). According to our plot for potential difference, Al and Ga doping makes $YMnO_3$ system to have better surface polarization and there exists an optimal doping ratio on the poling process. We caution that at the moment we cannot completely rule out a possibility of some effects due to direct charge injection during local electric switching and charge screening due to the correla-

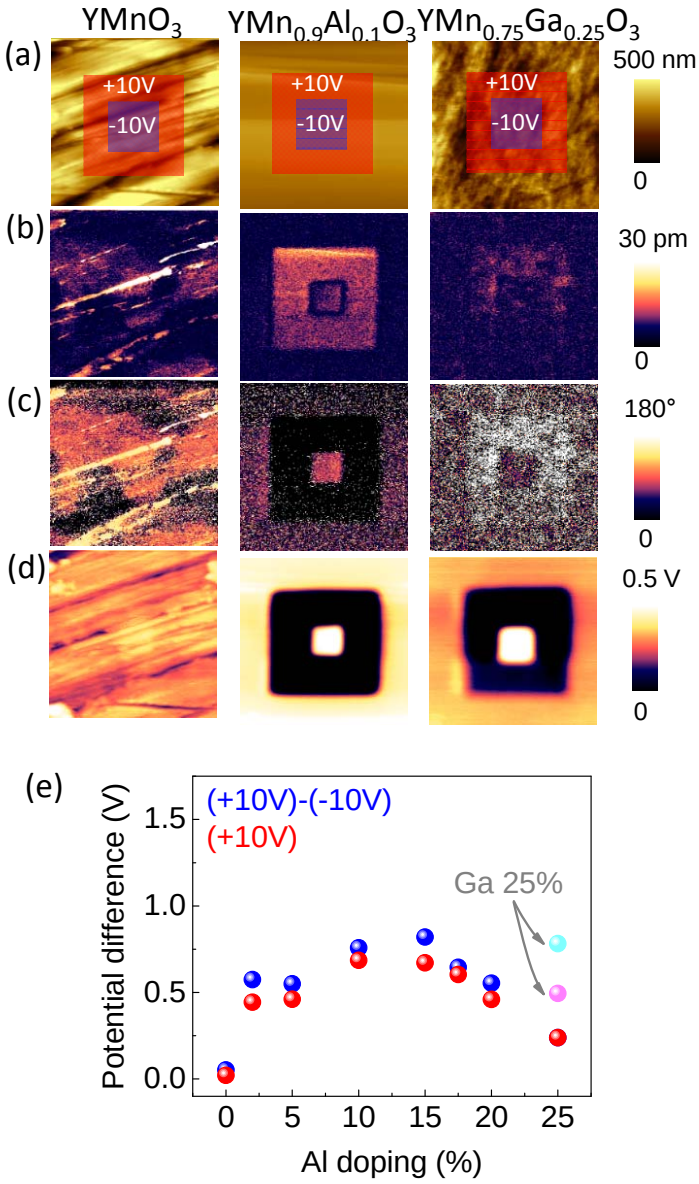

Figure 4.5: (a) It shows the surface topographic images, (b) and (c) PFM amplitude and phase signal, and (d) surface potential images from KPFM of three samples, $YMnO_3$ (1st column), $YMn_{0.9}Al_{0.1}O_3$ (2nd column), and $YMn_{0.75}Ga_{0.25}O_3$ (3rd column) after the applied biases over a square-shaped region of 1 μm $\times$ 1μm(-10 V, overlaid with blue) and 3 μm $\times$ 3 μm (+10 V, overlaid with red) at the central region. (e) Potential differences according to doping species and ratio, red ball presents a difference between +10V scanned area and not scanned, and blue ball is a difference between +10 V scanned area and -10 V area.

tion between ferroelectric polarization and ambient gas. Nevertheless, we are sure that our PFM and KPFM data are consistent with the conclusion drawn from the diffraction data that up to 10% of Al and 25% of Ga doping the samples remain ferroelectric.

4.4 Discussion and summary

When we discuss the doping effects of Al and Ga, a first factor to be considered is the fact that both Al and Ga disrupt the Mn network. If this is an important factor, then we would anticipate to see similar doping effects for both Al and Ga doping. However, the simple fact that we witnessed completely opposite doping effects on the transition temperature strongly indicate that this simple factor is not important. It is a very surprising result if one is reminded that MnO_5 titling was originally proposed as triggering the ferroelectric trasition [9]. Thus our observation seem to be sit against the original proposal and instead ask for different explanation. A second factor that can easily come to minds is the usual chemical pressure effects. We can count out again based on the experimental observation that at 50% doping of Ga the unit cell volume is more or less the same as 25% of Al doping as figure 4.1 (c) shows. Thus, if the chemical volume effect is the major factor, then again we cannot explain why our 50% Ga doped sample is still highly ferroelectric as undoped sample.

These considerations require us to look for other source for the experimental results. For this, we note that although Al and Ga have smaller ionic size than Mn the ionic size of Ga is a lot closer to that of Mn. Which basically means that there is much larger strain field generated around Al doping site as what is expected of Ga doping at the same doping level. We note that strain is known to suppress a ferroelectric transition. For example, the ferroelectric transition of $BaTiO_3$ thin film is strongly suppressed when strain was induced by controlling laser fluorescence during growth [33]. A further comment: although our observation of local strain effects of Al and Ga is generally consistent with this picture of strain on ferroelectricity, however it is a striking observation that such a strong ferroelectricity of h-$YMnO_3$ is completely destroyed by more than

15% Al doping. For this, we can think of the unusual triangular arrangement of Y and its geometrical frustration. To put it simply, we think that the observed drastic effects of Al as compared with Ga doping is the combined effects of local strain and geometrical effect.

To summarize, we investigated how Al and Ga doping at the Mn sites of $YMnO_3$ affects the ferroelectric transition by using powder and single-crystal diffraction technique together with PFM and KPFM measurements. By combining all the data, we conclude that the ferroelectric transition is disproportionately suppressed by Al doping and completely destroyed by more than 15% of Al doping. In contrast, the ferroelectric transition remain unaffected by up to 50% of Ga doping. We think that this strikingly different doping effects are the combined result of local strains induced doping together with geometrical effect of the triangular Y arrangement.

5. Nonmagnetic impurity doping effects on 2D triangular multiferroic Y(Mn, Al/Ga)O_3

Hexagonal manganite $RMnO_3$ shows multiferroic behavior, and it also hosts a two-dimensional (2D) triangular lattice of Mn moments, which itself is interesting from a magnetic standpoint as a 2D triangular lattice with antiferromagnetic interaction having strong frustrations. Generally doping perturbs the magnetic ground state, in this case with what is known as a 120° noncollinear antiferromagnet. Several theoretical studies in relation to this were reported, such as a Curie tail response due to impurities, magnetic textures, and changes to magnetic structures. We grew single crystals of $YMn_{1-x}(Al/Ga)_xO_3$, where Mn forms a 2D triangular lattice and Al and Ga become non-magnetic impurities, using a floating zone furnace and measured the physical properties. We found several interesting phenomena, such as the formation of a Curie tail, ferromagnetism at a low temperature and low energy excitation.

5.1 Nonmagnetic impurity doping effects on $YMnO_3$

Hexagonal manganite $RMnO_3$ has a two-dimensional (2D) triangular lattice, and shows a ferroelectric transition around T_C = 1200 K and an antiferro magnetic transition around T_N =70 K. Ferroelectric transitions were discussed in chapters 3 and 4. Because Mn ions have magnetic moments, they form 120° noncollinear antiferromagnets, and there have been several theoretical studies on the effects of nonmagnetic impurities on 2D triangular lattices.

Figures 5.1 (a) and (b) show Monte-Carlo simulation results from Wollny et al., who added a nonmagnteic impurity to a 2D triangular lattice. A non-magnetic impurity in a Heisenberg antiferromagnet rotates around other magnetic ions, as shown in figure 5.1(a), and it shows the formation of a Curie tail, shown in figure 5.1(b) at a low temperature [34].

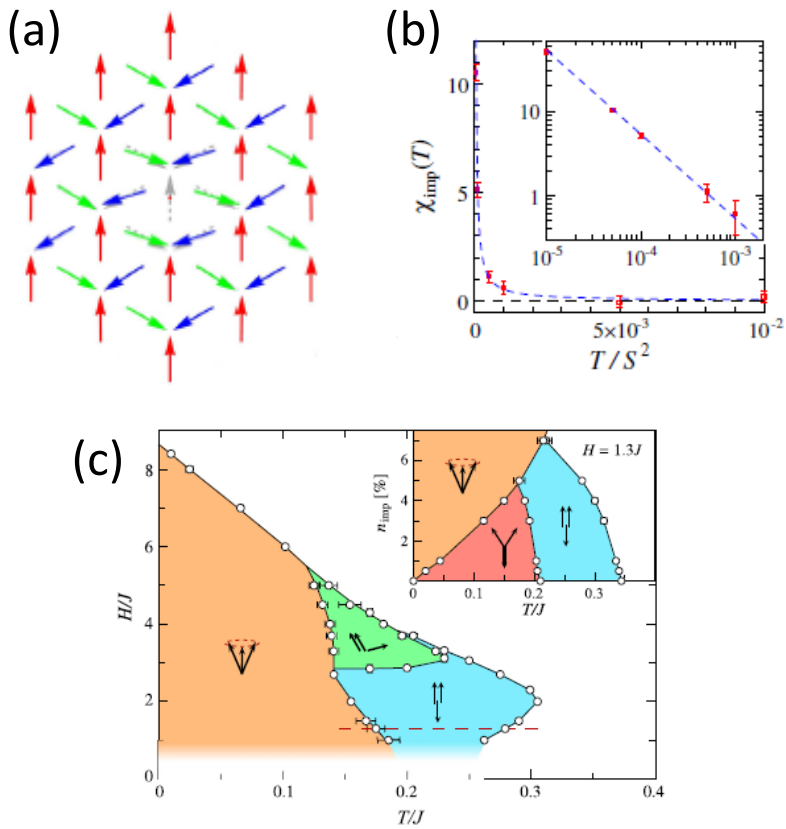

Figure 5.1: Previous study on non-magnetic impurity effects on triangular lattice. (a),(b) Impurity contribution on magnetization will behave as a Curie tail at low temperature [34]. (c) Magnetic phase diagram depends on field and temperature with 5% impurity on 2D triangular lattice [35].

Recently, Maryasin et al. reported a phase diagram of a magnetic structure with 5% nonmagnetic impurity doped onto a triangular lattice according to a Monte-Carlo simulation, as shown in figure 5.1(c). Changing the impurity ratio and magnetic field modify magnetic structure from the original 120° antiferromagnet [35] with the possibility of ferromagnetism.

Several experiments related to the doping of Ga on h-$YMnO_3$ have been reported. It was shown that the thermal conductivity, magnetic susceptibility and dielectric constant change as the doping ratio is increased [36–38]. Neutron diffraction experiments up to a doping ratio of 10% were also studied [32]. Nonetheless, as noted above, interesting phenomena such as spin textures, Curie tails and magnetic structural changes, predicted by theoretical calculation have not been studied in depth.

To study nonmagnetic impurity effects on a 2D triangular magnetic lattice, h-$YMn_{1-x}(Al/Ga)_xO_3$ samples were grown using a floating zone furnace as explained in section 4.2. The magnetic properties and heat capacity were measured and analyzed. Additionally, neutron diffraction studies for magnetic structural analysis (as explained in section 2.2.3) were performed.

5.2 Physical property changes on doping with non magnetic atoms

Figure 5.2 shows susceptibility measurements results on (a),(b) h-$YMn_{1-x}Al_xO_3$ and (c) h-$YMn_{1-x}Ga_xO_3$. One of the noticeable results is a decrease of magnetic transition temperature. The peak near 70 K is a sign of magnetic transition, and it decrease as the doping ratio of Al or Ga increases. The magnetic transition temperature, T_N is also shown in figure 5.4.

Another notable point is the increase in the formation of a Curie tail. As predicted in Wollny et al. [34], the susceptibility increase at a low temperature as the doping ratio increases for both Al and Ga doping. The temperature dependence of the susceptibility at a low temperature takes the form of a Curie tail for highly doped case.

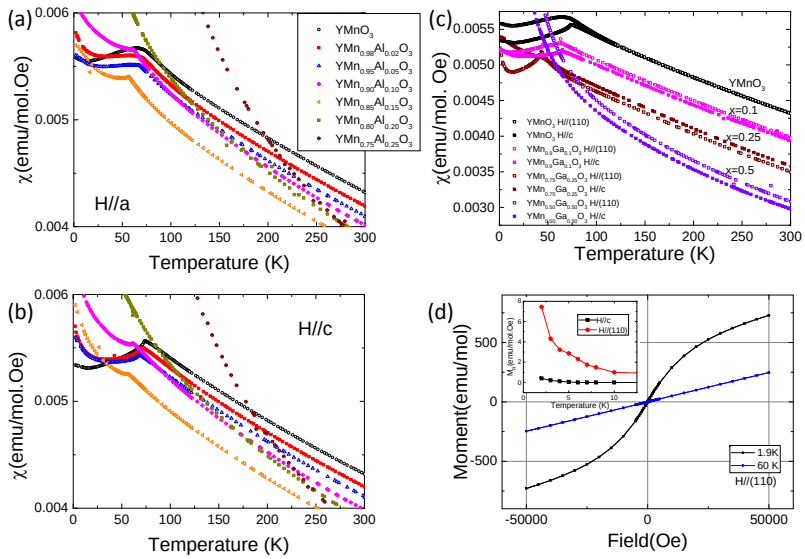

Figure 5.2: Susceptibility on h-$YMn_{1-x}Al_xO_3$ along (a) (110) direction and (b) c-axis. (c) Susceptibility on h-$YMn_{1-x}Ga_xO_3$. (d) Magnetic moment depends on field on h-$YMn_{0.5}Ga_{0.5}O_3$ which show ferromagentism.

Another point is the tendency of change of the temperature dependence below the magnetic transition. Magnetic susceptibility decreases suddenly immediately below the magnetic transition point, and the amount of the decrease is greater along the c- direction in the pure case. But as the doping ratio increases, the amount of the decrease along the (110) direction becomes greater. This suggests that the interaction between the magnetic atoms and the magnetic ordering changes.

The last point is ferromagnetism, as shown in figure 5.2(d). Interestingly, ferromagnetism is greater along the 110 direction for highly doped samples. Ferromagnetism also appears along the c direction, but it is weak. In the case of Al doping, more than 20% of doped samples have ferromagnetism, whereas for Ga doped case 50% of the samples demonstrate ferromagnetic behavior. These phenomena will be discussed later.

Figure 5.3 and 5.4 show the physical parameters as calculated from figure 5.2. As the doping ratio increases, the magnetic transition temperature decreases and the Curie-Wises temperature increases. Thus the frustration factors remain unchanged or even increase. For the highly doped cases ($YMn_{0.75}Al_{0.25}O_3$ and $YMn_{0.5}Ga_{0.5}O_3$), the mag-

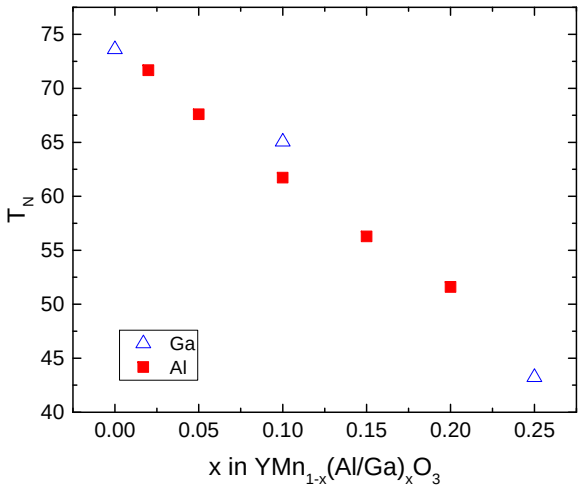

Figure 5.3: Magnetic transition temperature measured from susceptibility measurements

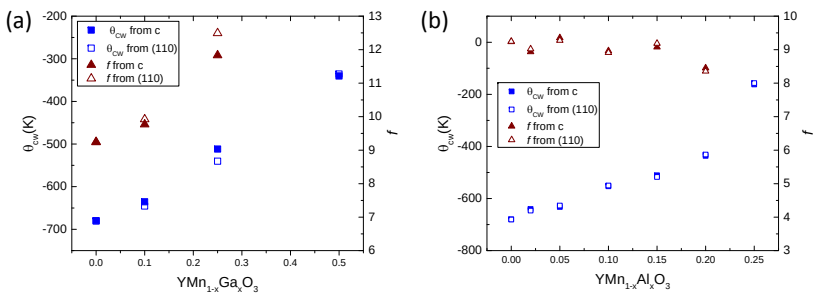

Figure 5.4: Curie-Weiss temperature and frustration factor are calculated from susceptibility measurements.(a) h-$YMn_{1-x}Al_xO_3$ and (b) h-$YMn_{1-x}Ga_xO_3$

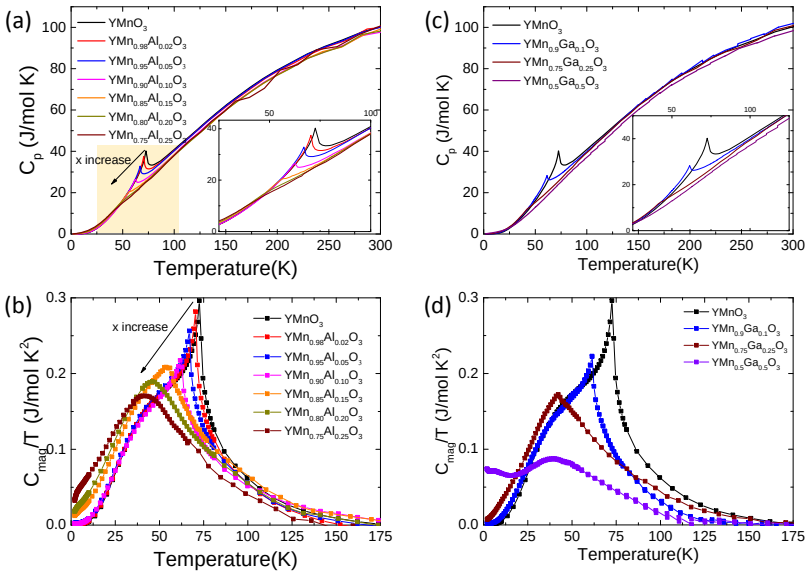

Figure 5.5: Heat capacity and C_{mag}/T depends on temperature. (a),(b) h-$YMn_{1-x}Al_xO_3$ and (c),(d) h-$YMn_{1-x}Ga_xO_3$

netic transition temperatures are difficult to determine.

The heat capacity measurements results are shown in figure 5.5. Similar to the magnetic susceptibility measurements result, the magnetic transition temperature decreases as the doping ratio increases. Interesting points are found at C_{mag}/T in figures 5.5(b) and (d). C_{mag}/T values were calculated by subtracting the phonon parts, using a two Debye temperature model [30]. There are sharp peaks and a broad hump at a low temperature, where the peak intensity decreases while the hump remains as the doping ratio increases. As the doping ratio increases, the low temperature C_{mag}/T value increases and shows a non-zero value. It is believed that the broad hump is related to the magnon contribution and that the non-zero C_{mag}/T value is related to low energy excitation. Inelastic neutron scattering can be used to clarify the question. Similar to the magnetism results, comparing the h-$YMn_{0.75}Al_{0.25}O_3$ and h-$YMn_{0.75}Ga_{0.25}O_3$ results shows that doping with Al has a greater effect on the heat capacity at a low temperature than doping with Ga.

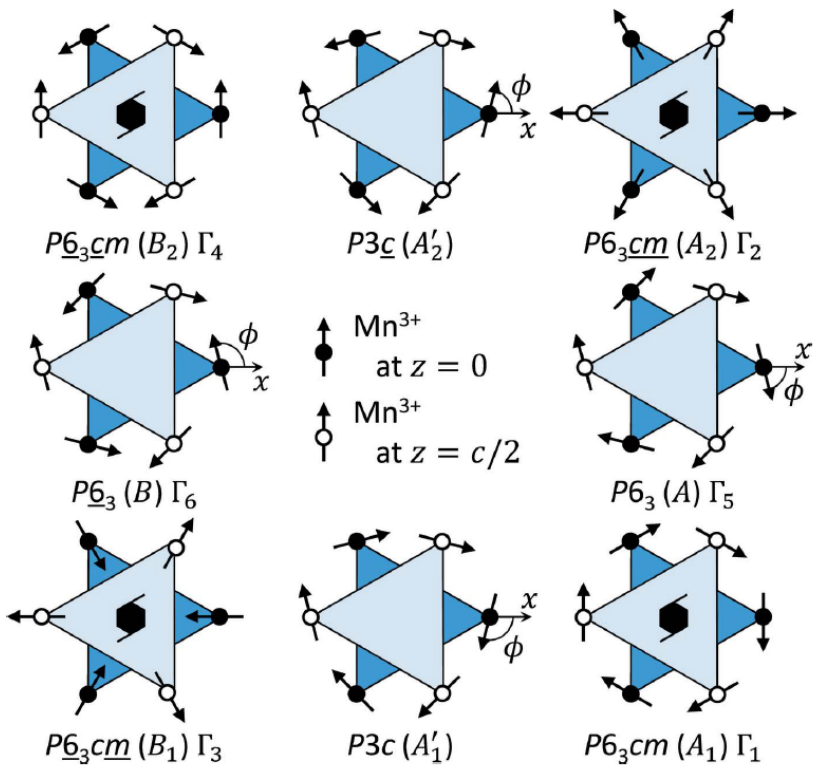

Figure 5.6: Possible magnetic structure for propagation vector **k** = (0,0,0) [13]

5.3 Magnetic structures

H-$YMnO_3$ shows long range magnetic ordering; therefore the doping effects are of interest in relation to magnetic structural changes. As the heat capacity data show only a broad hump in highly doped systems, it is necessary to check whether long range ordering exits or not. We performed low temperature neutron diffraction experiments on h-$YMnO_3$ at HANARO and on $YMn_{0.8}Al_{0.2}O_3$ at ANSTO.

Using a magnetic structural analysis as explained in section 2.2.3, we can determine the possible magnetic structures for the propagation vector **k** = (0,0,0), as shown in figure 5.6. Due to symmetry, only Γ_2 can have ferromagnetism along the c-direction.

The neutron diffraction results are shown in figure 5.7. We found magnetic Bragg peaks, indicating that there is long range ordering even

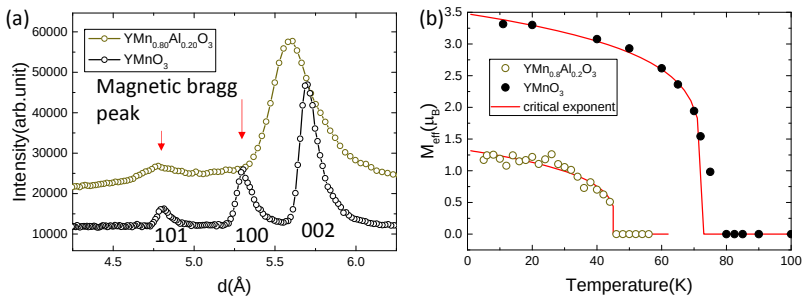

Figure 5.7: (a) Neutron diffraction experiment results on $YMnO_3$ and $YMn_{0.8}Al_{0.2}O_3$. (b) Magnetic effective moments calculated by neutron diffraction experiments.

in highly Al doped samples. The magnetic effective moment decreases greatly in the h-$YMn_{0.8}Al_{0.2}O_3$ case by as much as one third of the decrease in the pure h-$YMnO_3$ case. As the magnetic Bragg peaks intensity changes, the magnetic structure also changes from Γ_3 to Γ_4.

However the changes in the magnetic structure is not merely a simple change from Γ_3 to Γ_4. As shown in the magnetic susceptibility results, we found ferromagnetism in the ab plane direction, which is not allowed by the magnetic symmetry. As predicted earlier work [35], this suggests a change in the magnetic structure from the original antiferro magnetic 120° ordering structure. The one third suppression of the effective moment and low energy excitations at heat capacity may also be connected.

Doping h-$YMnO_3$ with Al and Ga ions shows different outcomes. Because Al^{3+} and Ga^{3+} are both non magnetic, the effects should be identical in an ideal case. However as noted in chapter 4, the ionic size difference between Ga^{3+} and Mn^{3+} is much larger in the Al^{3+} and Mn^{3+} case, for which the strains are also additionally affected.

Current magnetic structural analysis methods focus on h-$YMnO_3$ and h-$YMn_{0.8}Al_{0.2}O_3$. We found that there are magnetic structure differences between them. Additional experiments would be needed to determine how the magnetic structure changes between these two magnetic structures, and how Ga doping would affect the magnetic structure. We could also compare these results with the theoretically predicted phase diagram [35].

5.4 Summary

We successfully grew single crystals of $YMn_{1-x}(Al/Ga)_xO_3$ using a floating zone furnace. Non-magnetic doping on a 2D triangular lattice affects several physical properties, such as the magnetization and heat capacity. We found several interesting impurity effects, such as an increased Curie tail, low energy excitation, and ferromagnetism in this system. Further work is needed for a more in-depth study of the magnetic structures study.

6. High-resolution structure studies and magnetoelectric coupling of relaxor multiferroic $Pb(Fe_{0.5}Nb_{0.5})O_3$

$Pb(Fe_{0.5}Nb_{0.5})O_3$ (PFN) is one of the few relaxor multiferroic systems with perovskite structure, and it has a G-type antiferromagnetic transition at T_N = 143 K and a ferroelectric transition at T_C = 385 K. Though importance of suitable candidate material for multilayer ceramic capacitors due to its high dielectric constant, the crystal structure has remained unsettled. By using high-resolution neutron-diffraction experiments, we confirmed the structure below T_C as *Cm*. We also paint a comprehensive picture of the long- and short-range structures of PFN: (i) a clear sign of short-range structural correlation above T_C, (ii) no sign of the negative thermal expansion behavior reported in a previous study and well fitted with Debye-Grüneisen formula, and (iii) clearest evidence thus far of magnetoelectric coupling below T_N. We conclude that the unusual relaxor multiferroic behavior are due to the disorder between Fe^{3+} and Nb^{5+} atoms. We argue that this disorder gives rise to short-range structural correlations arising from O disorder in addition to Pb displacement.

6.1 Relaxor multiferroic $Pb(Fe_{0.5}Nb_{0.5})O_3$

It is rare that a single system which hosts two or more ordered ground states out of otherwise unconnected degrees of freedom in nature. If there are multiple ordered ground states, a natural question to ask is whether they are connected to one another. Although the same electrons may be responsible for multiple degrees of freedom, allowing coupling of the various forms of order, this is uncommon, making materials in which they are coupled particularly interesting. Magnetoelectric multiferroic materials, in which ferroelectricity and magnetism coexist and are coupled, are an example of just such a material. The ability to control one form of order via another offers a huge potential for technological applications and, at the same time, poses new challenges for our

understanding of how distinct degrees of freedom as disparate as bulk polarization and magnetization can be coupled to one another [39, 40]. Here the sought-after coupling, so-called magnetoelectric effects, can lead to better manipulation of unusual multiferroic behavior and to exotic excitations of mixed character. Despite the huge interest, however, the origin of magnetoelectric coupling has often difficulty experimentally for a given material.

Lead iron niobate $Pb(Fe_{0.5}Nb_{0.5})O_3$ (PFN) is a multiferroic material with a ferroelectric transition at T_C = 385 K [41] and an antiferromagnetic transition at T_N = 143 K [41–44] which is known to be a G-type [45]. It is noteworthy for its high dielectric constant, which changes at both the ferroelectric [42, 46, 47] and the magnetic transitions [41, 47, 48] and is strongly frequency dependent. Its reported high dielectric constant makes it a suitable candidate material for multilayer ceramic capacitors among other electronic devices. The reported strong frequency dependence, making it a rare example of a relaxor multiferroic, most likely arises from disorder at the magnetic B site of the perovskite structure. Since many ferroelectric systems have disordered magnetic ions on the B site, a full understanding of PFN might well have wider implications for finding or optimizing other relaxor multiferroic materials for potential applications.

Relaxor ferroelectrics are ferroelectric materials that show high electrostriction. Electrostriction is a property of all dielectric materials, and it is caused by a slight displacement of ions in the crystal lattice upon being exposed to an external electric field.

Despite the interest in the physical properties of PFN, however, several features of the underlying crystal structure still remain unresolved. For example, two competing space groups, $R3m$ [45] and Cm [49, 50], have been proposed for the low-temperature structure. The two structure are shown in Figure 6.1. Fe/Nb are surrounded by oxygen octahedral and Pb are studied in between. Figure 6.1 (a) shows cubic $Pm\bar{3}m$ structure which is the structure above T_C. The two structure in figures 6.1(b) and (c) differ in terms of how they are tilted and shifted from a cubic structure [51].

Another remaining problem is about the report of negative thermal

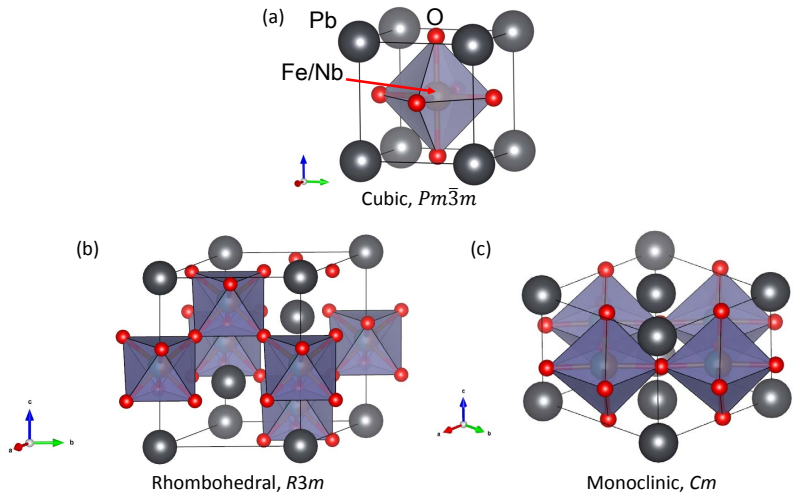

Figure 6.1: (a) Cubic $Pm\bar{3}m$, (b) Monoclinic Cm and (c) Rhombohedral $R3m$ structure.

expansion below the antiferromagnetic transition [49]. They observed the total volume expansion below T_N as temperature goes down which is not following the Debye-Grüneisen formula [52].

In attempting to characterize the relaxor behavior, several groups have investigated the local structure [53, 54], which is closely associated with relaxor behavior in ferroelectrics, and discussed the possibility of structural disorder both experimentally [54, 55] and theoretically [56]. Despite these studies, the key questions have yet to be fully answered. For instance, it will be interesting to know how the relaxor behavior is connected to the short-range local structure. More importantly, one first has to know the exact details of the local distortion and, if possible, the structural basis of the sought-after magnetoelectric coupling. We performed neutron total scattering to study on local structure in better resolution.

In order to address these questions, we have undertaken full high-resolution neutron powder-diffraction studies as well as total scattering experiments using two state-of-the-art instruments: S-HRPD and NOVA, both at J-PARC, in Tokai, Japan. For this kind of study it is essential to be able to examine both long- and short-range structures simultaneously as performed for other ferroelectric materials [57]. By combin-

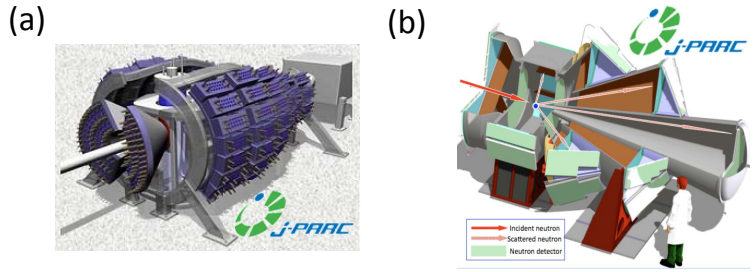

Figure 6.2: (a) S-HRPD beam line (b) NOVA beamline

ing data obtained from both instruments, we conclude that the low-temperature space group is Cm with clear signs of the short-range structure surviving even above the ferroelectric transition temperature, offering an explanation for the relaxor behavior. Neither experiment showed signs of negative thermal expansion. We then uncovered structural signatures of the magnetoelectric coupling by analyzing the temperature dependence of the electric polarization calculated from the structure parameters. Our detailed analysis of the local structure leads us to the conclusion that both Pb displacement and O disorder are exhibited in this material.

6.2 Experimental details

About 7 g of polycrystalline PFN samples were prepared by a standard solid-state method. Stoichiometric PbO, Fe_2O_3, and Nb_2O_5 were mixed, then calcined in air at 850 °C for 2 days. After calcination the products were ground, pressed into pellets, and then sintered at 1050 °C for 1 day. The samples were verified to be single phase with a Rigaku Miniflex II x-ray diffractometer as well as the later high-resolution neutron diffraction studies which form the main body of this paper. Magnetic susceptibility were measured by MPMS and T_C and T_N were confirmed.

High-resolution neutron time-of-flight powder-diffraction experiments were carried out using the S-HRPD beamline at J-PARC, Tokai, Japan, on a powder sample in a cylindrical vanadium can, at ten temperatures from 10 to 300 K. The beam line images are shown in figure 6.2. Rietveld

refinement of the diffraction data was performed using FULLPROF [25]. The subsequent total scattering experiments were carried out using a vanadium-nickel sample can at the NOVA beamline at J-PARC with a maximum Q value of $Q_{max} = 30$ Å^{-1} at five temperatures between 62 and 453 K. Sample environment constraints prevented measurements above the ferroelectric transition temperature at S-HRPD, so NOVA was also used to collect diffraction patterns at selected higher temperatures. For the local structure study, a radial distribution function was calculated from the total scattering data and analyzed using PDFGUI [5]. The experimentally obtained $S(Q)$ was then Fourier transformed into real space to obtain the atomic pair distribution function $G(r)$ as follows:

$$G(r) = 4\pi r\left[\rho(r) - \rho_0\right] = \frac{2}{\pi}\int_0^{Q_{max}} \left[S(Q) - 1\right] \sin Qr \, dQ,$$

where $\rho(r)$ and ρ_0 are the atomic number density and the average number density, respectively, and Q_{max} is the maximum scattering wave vector. $G(r)$ was modeled using $4 \times 4 \times 4$ supercells for several different models of the short-range structure. The detailed methods of using software were discussed in chapter 2.2.1 and 2.2.2.

6.3 Structure determination

The low-temperature space group of PFN is thought to be the monoclinic space group Cm, but as discussed in chapter 6.1, the $R3m$ space group has also been proposed as an alternative structure. To the best of our knowledge it is still not determined which one of the two space groups is correct. Figure 6.3(a) shows the neutron powder-diffraction pattern and its refinement results in the Cm and $R3m$ (inset) space groups at 300 K. We assumed that Fe and Nb are randomly distributed at the same crystallographic position [45, 49, 50] and allowed this sublattice to shift relative to Pb but did not split any sites at this stage. Satisfactory refinements have previously been reported in both $R3m$ [45] and Cm [49]; we rely on an additional approach to distinguish these space groups. The data are well explained by both structures, although the quality of the refinement is slightly better in Cm, but this is not surprising since

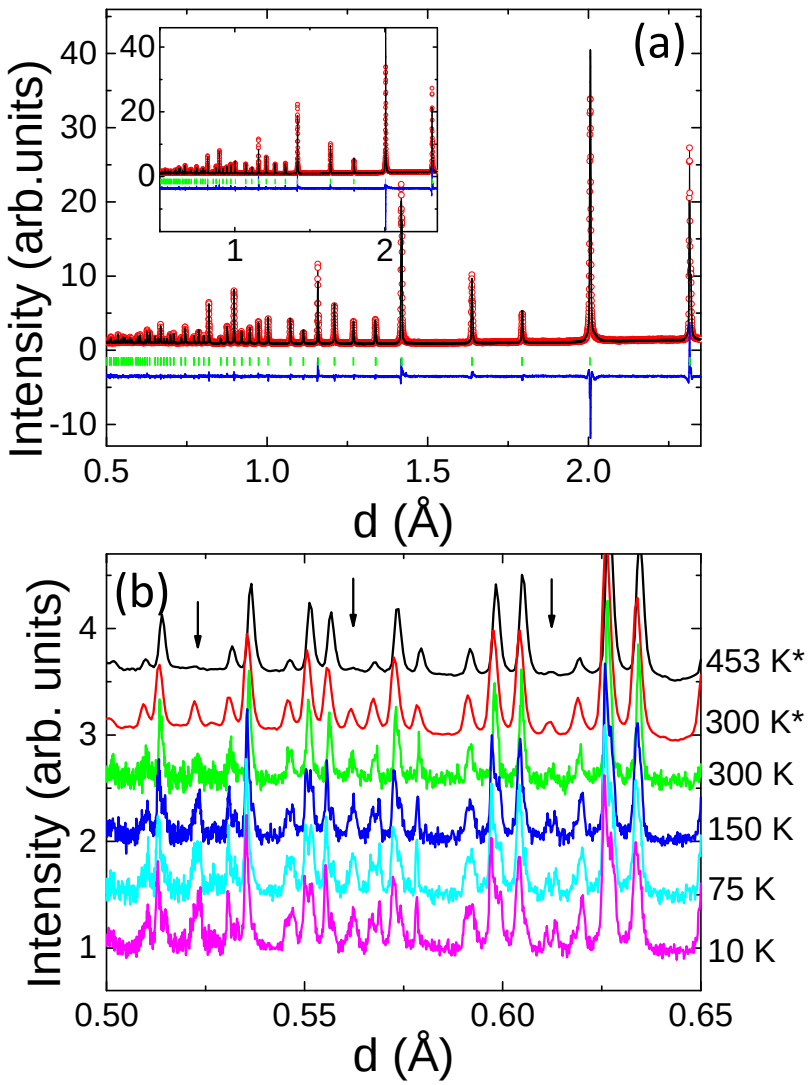

Figure 6.3: (a) Neutron powder-diffraction patterns with refined results in the Cm and $R3m$ (inset) space groups, respectively, at 300 K. Circles represent data, a line the refinement, and the line at the bottom the residual, whereas green vertical bars mark the Bragg positions. (b) Diffraction patterns at several temperatures. The upper two datasets (starred) are NOVA results, and the others are S-HRPD results. Several peaks disappear above T_C = 385 K due to the structural transition (arrows).

Table 6.1: Refined structure parameters at 300 K in the Cm (with b as the unique monoclinic axis and cell choice 2) and $R3m$ structures. The unsplit Pb position is taken as the origin in Cm, whereas the Fe/Nb position is set to (0.5,0.5,0.5) for $R3m$ to aid comparisons to the literature.

Cm	$a_m = 5.6819(1)$ Å, $b_m = 5.6738(1)$ Å, $c_m = 4.01202(5)$ Å, $\beta = 89.896(2)^\circ$			
Ions	x	y	z	B (Å^2)
Pb	0.0000	0.0000	0.0000	1.82(8)
Fe/Nb	0.4669(9)	0.0000	0.5165(18)	0.34(3)
O1	0.4333(13)	0.0000	0.0002(26)	0.54(3)
O2	0.2129(20)	0.2483(7)	0.4989(29)	0.54(3)
R_p: 5.26, R_{wp}: 7.68, R_{exp}: 4.13, χ^2: 3.45				
$R3m$	$a_r = 4.01389(3)$ Å, $\alpha = \beta = \gamma = 89.9223(2)^\circ$			
Pb	0.0205(6)	0.0205(6)	0.0205(6)	2.45(5)
Fe/Nb	0.5000	0.5000	0.500	0.27(2)
O	0.4772(2)	0.4772(2)	-0.0092(5)	0.58(2)
R_p: 5.48, R_{wp}: 8.01, R_{exp}: 4.13, χ^2: 3.76				

the Cm structure model has more free parameters. Table 6.1 summarizes the refined structural parameters for the 300 K data in the Cm and $R3m$ structures. Both differ in how they are tilted and shifted from the cubic structure [51], and both are fitted well. Results are described in the rhombohedral setting of the $R3m$ structure for comparison with Ref. [45]. One can also convert the lattice parameters of the Cm structure to pseudocubic notation for ease comparison with the paraelectric structure as performed in Fig. 6.1(c) [1].

In the temperature-dependent data, magnetic peaks can be observed at $d = 1.55$ and 1.85 Å, consistent with the reported G-type antiferromagnetic structure [45]. Several structural peaks, shown in Fig. 6.3(b), are absent above the ferroelectric transition of 385 K as seen comparing the data taken at 453 and 300 K; these peaks are marked by arrows. We note that we can refine the highest temperature data in the paraelectric phase using the previously reported space group $Pm\bar{3}m$ [50, 55, 58];

[1] Multiplying by the matrix $\begin{pmatrix} 1/\sqrt{2} & 1/\sqrt{2} & 0 \\ -1/\sqrt{2} & 1/\sqrt{2} & 0 \\ 0 & 0 & 1 \end{pmatrix}$ converts the monoclinic structure to the pseudocubic structure.

however, as we will discuss later, there are clear signs of short-range structure in the total scattering data even at 453 K.

Since refinement cannot distinguish two structure, new method was needed. In order to distinguish the two candidate low-temperature space groups, the temperature dependence of the peak widths for several nuclear Bragg peaks as obtained from fits to a Lorentzian line shape was examined. And a search was performed for peaks that are split in one space group but not the other. The large number of reflections in this low-symmetry structure makes it difficult to find nonoverlapping peaks, but several good candidates were located. The (002) and (220) Bragg reflections of the Cm structure, shown in the inset of Fig. 6.4(a), were found to be the most suitable: In the $R3m$ space group the resulting peak contains only one unique reflection, (200). No clear splitting is observed at low temperatures, but the peak width increases markedly on cooling as shown in Fig. 6.4(a), which is exactly opposite to what one expects from any conventional thermally activated broadening process. Similar temperature dependence is observed in other peaks, which are split in Cm and not in $R3m$. As we cannot find a peak from a well-separated Bragg reflection in our data because of the low symmetry, we choose $SrRuO_3$ measured under almost identical conditions in order to demonstrate how the width of a single Bragg peak behaves as a function of temperature when measured at the S-HRPD beamline. In Fig. 6.4(a), we plotted the (022) peak of $SrRuO_3$ [59] where the width of the single Bragg peak remains temperature independent over the measured temperature range as expected. The unusual peak broadening seen in the (002)/(220) peak of PFN is naturally explained by a splitting of two reflections, which strengthens on cooling, and would appear to exclude the $R3m$ structure. The origin of this unusual temperature dependence can be found by examining the Fe/Nb–O bond lengths and their temperature dependence, shown in Fig. 6.4(b).

By concluding structure as Cm, we could get several lattice parameters. The temperature dependence of the lattice constants and unit-cell volume are summarized in Fig. 6.5. We also plot the monoclinic angle in pseudocubic notation. Square symbols represent NOVA results, whereas red circles indicate those from S-HRPD. Refinements were performed in

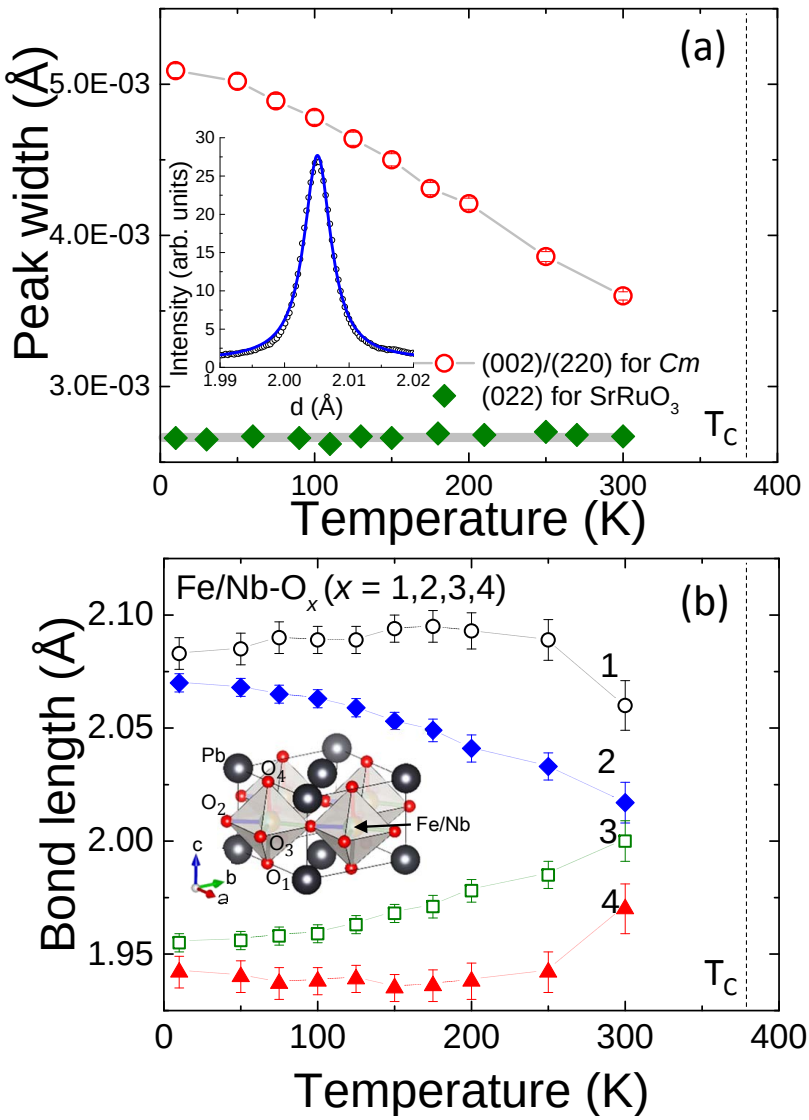

Figure 6.4: (a) Temperature dependence of the peak width of the (002)/(220) Bragg peak in the Cm structure with the raw data at 10 K shown in the inset. Error bars are smaller than the symbol size. The data for the (022) peak of $SrRuO_3$ were taken after Ref. [59] (see the text). (b) Temperature dependence of Fe/Nb–O bond lengths. The inset depicts the structure of PFN with the Cm space group all data taken from S-HRPD: There are four different Fe/Nb–O bonds denoted by the numbers.

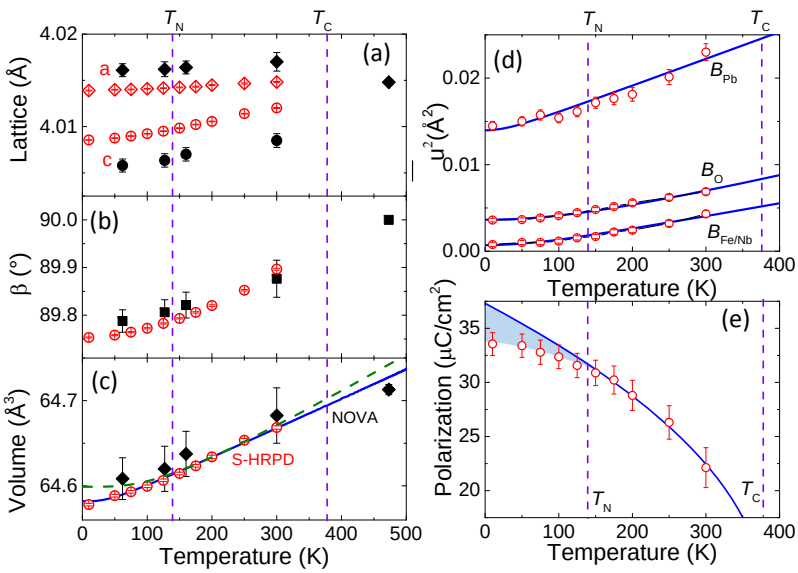

Figure 6.5: Temperature dependence of (a) lattice parameters, (b) monoclinic angle, (c) unit-cell volume, (d) thermal parameter, and (e) calculated polarization. The refined unit-cell volume (symbols) is shown together with the theoretical curve obtained from the Debye-Grüneisen formula, and polarization was calculated from the refined atomic positions.

the $Pm\bar{3}m$ structure above T_C and the Cm structure below T_C. Both the lattice constants and the unit-cell volume follow a consistent trend without any clear anomaly at the antiferromagnetic transition. Regarding the previous claim of negative thermal expansion [49], we note that there is no evidence of such an effect in the data presented here, taken using either instrument, although it is also important to note that lattice parameters from x-ray diffraction are normally more precise. It is an open question to us why our data collected from two different instruments do not show the negative thermal expansion claimed in Ref. [49].

In order to further analyze the temperature dependence of the unit-cell volume, the Debye-Grüneisen formula [52] was used

$$V(T) = \frac{V_0 U(T)}{Q - bU(T)} + V_0, \tag{6.1}$$

$$U(T) = 9Nk_BT\left(\frac{T}{\Theta_D}\right)^3 \int_0^{\frac{\Theta_D}{T}} \frac{x^3}{e^x - 1} dx, \tag{6.2}$$

where $U(T)$ is total internal energy, $Q = V_0 B_0/\gamma$, $b = (B_0' - 1)/2$, γ is the Grüneisen parameter, B_0 and B_0' are the bulk modulus and its first derivative with pressure, N represents the number of atoms in the unit cell, k_B is the Boltzmann constant, and V_0 is volume at zero temperature. Fitting (shown by a solid line) results in a Debye temperature Θ_D of only 150 K, whereas $b = 1.5$, $V_0 = 64.582$ Å^3, and $Q = 3.87(6) \times 10^{-17}$ J are similar to parameters used for other materials [60–62]. We note that the resulting Debye temperature is abnormally small, leading to a bulk modulus around 600 GPa for a typical Grüneisen parameter of order one, which is high for an oxide material: For example, we earlier found bulk modules of 120 GPa for $YMnO_3$ [63] while 250 GPa has been reported for $MgSiO_3$ [64]. Note that this assumption about the Grüneisen parameter is crude, and so our estimate of the bulk modulus should be taken with caution. Moreover a true test of the bulk modulus needs to be performed by measuring the volume measurement under pressure. On the other hand, fixing the Debye temperature to the more typical 430 K led to a noticeably poorer fit (dashed line) with $b = 1.5$, $V_0 = 64.595$ Å^3, and $Q = 2.9(1) \times 10^{-17}$ J. This could be consistent with an anomaly below T_N but opposite in sign to that reported previously.

Figure 6.5(d) shows the temperature dependence of atomic displacement parameters $\overline{u^2}$ for each atom. The thermal parameter of Pb is much larger than those of O and Fe/Nb, almost comparable to those of other Pb-containing ferroelectric materials [50] and consistent with a previous report [54]. The temperature dependence was modeled using

$$\overline{u^2} = \left(\frac{145.55T}{M{\Theta_D^i}^2}\right)\varphi\left(\frac{\Theta_D^i}{T}\right) + A^i \tag{6.3}$$

$$\varphi\left(\frac{\Theta_D^i}{T}\right) = \frac{T}{\Theta_D^i}\int_0^{\frac{T}{\Theta_D^i}} \frac{x}{e^x - 1}dx, \tag{6.4}$$

where i represents each atomic species (Pb, Fe/Nb, O), and $A^i = 36.39/M^i\Theta_D^i$ is related to zero-point energy of the atoms concerned with atomic mass M^i[52]. However, it was necessary to add constant offsets to A to achieve better agreement. The final result, denoted by lines in Fig. 6.5(d), indicated effective Debye temperatures of 150 K for Pb, 680 K for O, and 370 K for Fe/Nb.

Using the structural information, we then searched for possible experimental evidence of magnetoelectric coupling. PFN is known to exhibit a frequency-dependent anomaly in the dielectric constant at T_N, but little else is known of the magnetoelectric coupling. From the high-accuracy structural information presented here, it is possible to calculate the expected ferroelectric polarization, starting from the centrosymmetric $Pm\bar{3}m$ space group. Using a similar approach, we were previously able to show a negative magnetoelectric coupling in one of the best-studied multiferroic compounds, $BiFeO_3$ [65]. For simplicity, the nominal valences of the atoms were used as a starting point: Pb^{2+}, Fe^{3+}, Nb^{5+}, and O^{2-}. Since the actual valences, so-called Born effective charges, which include dynamic terms, might well differ from the nominal charge values [66], the discussion below may not be fully quantitative, but it should be qualitatively correct. Using the above assumptions, the electric polarization was calculated with respect to the paraelectric $Pm\bar{3}m$ phase. As shown in Figure. 6.5(e), the estimated polarization at room temperature is around 20 $\mu C/cm^2$, which is twice that reported [41, 42] in polycrystalline samples. Considering the rough assumptions made and the fact that the experiments were performed on powder samples,

we consider this degree of deviation acceptable. The temperature dependence was then parametrized using Ginzburg-Landau analysis, assuming that the electric polarization follows the usual first-order temperature dependence: $F(P) = \frac{\alpha_2}{2}P^2 + \frac{\alpha_4}{4}P^4 + \frac{\alpha_6}{6}P^6$, where F is the Ginzburg-Landau free energy and P is the polarization. A fit to all points produced an unphysically high Curie temperature, whereas constraining the Curie temperature led to clear systematic trends in the residuals; a fit to only the points above the Néel transition, shown in Fig. 6.5(e), predicted a Curie temperature of 380 K in close agreement with experiment, but the data appear to deviate from this fit below T_{N}. This discrepancy, marked by shading in the figure, is the clearest experimental evidence yet of the magnetoelectric coupling in PFN.

6.4 Local structure study

For further analysis of the short-range structure, Figure. 6.6(a) shows how the radial distribution function $G(r)$ calculated from the NOVA data changes gradually with temperature. Of note are the several regions where peaks' intensities increase on cooling. At these short length scales, corresponding to large momentum transfers Q, we can ignore contributions from magnetic scattering because they are usually small compared to nuclear scattering [67]. As shown in Fig. 6.6(b), the long-range structure up to 100 Å can be well explained by the structure based on Cm space group(solid line).

First, we consider the short-range structure at high temperatures above the ferroelectric transition. Using data taken at 453 K, we tested four different models to explain the data and clarify the local structure as shown in Figure 6.7, all variants of the $Pm\bar{3}m$ structure. All of these outcomes are explained in more detail below: (A) one without local short-range structure, (B) one with Pb displacements as considered previously [54], (C) one with Pb disorder, and (D) one with both Pb displacement and O disorder. For all models, Fe and Nb are treated as an average pseudoatom as in the refinement. Models B–D take model A as their starting point and allow additional freedom in the atomic positions. In departing from model A, C centering was not retained. As shown in

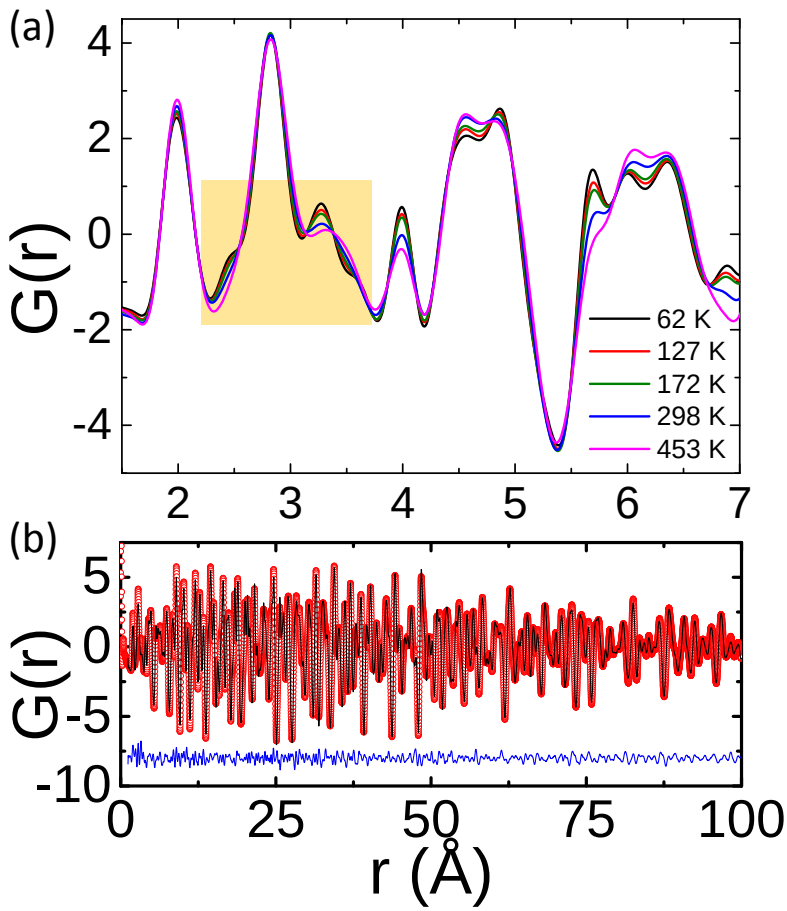

Figure 6.6: (a) Radial distribution function $G(r)$ at several temperatures, calculated from NOVA results. Gradual changes may be observed with temperature at several regions of interest. (b) Radial distribution function $G(r)$ is compared with fitting results over a wide length-scale range for the 62 K data. The symbols represent the data points, whereas the line is the fitting results with the difference curve shown at the bottom.

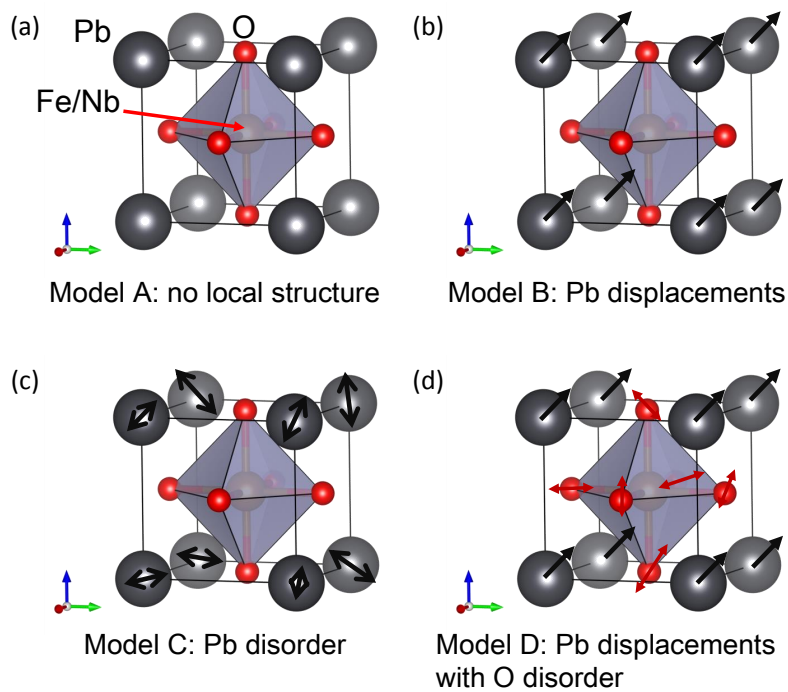

Figure 6.7: Local structure models: Model A assumes no local structure; model B assumes Pb displacements; model C considers Pb disorder; and model D combines Pb displacements with O disorder. Arrows show direction of atom movements(Supercell are not shown).

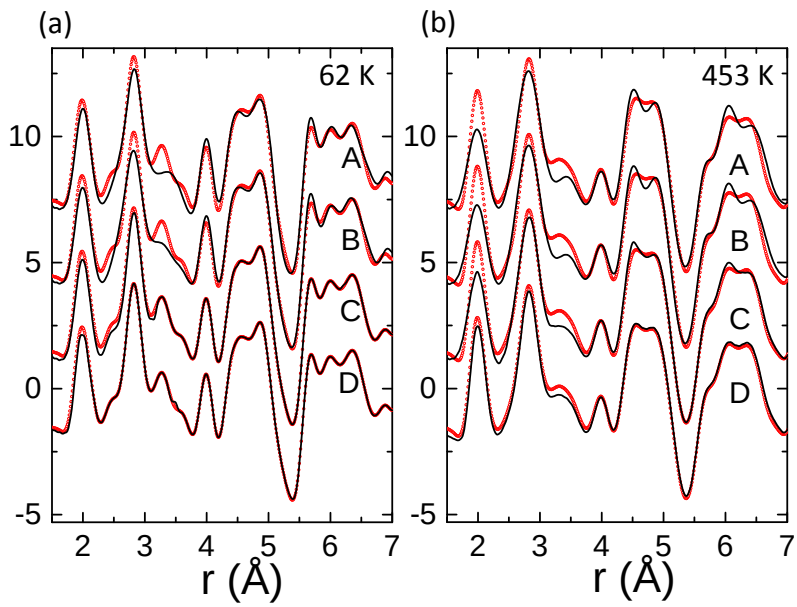

Figure 6.8: The local structure is compared with several models at (a) 62 K and (b) 453 K. Circles are calculated from experimental data, and lines are fits to several models explained in Figure 6.7. Traces have been offset vertically for clarity.

Fig. 6.8(b), the agreement is indeed improved by including Pb displacement and O disorder in our model calculation. Upon closer inspection, model A is found not to satisfactorily explain the intensities of peaks at $r = 2$ and $r = 3.5$ Å, and agreement with experimental results is poor at longer distances. It is particularly surprising that, even in the nominally paraelectric phase well above the ferroelectric transition, there is clear evidence of short-range structure. We note that similar behavior is often found in relaxor ferroelectric materials [3, 68]. Thus, our result adds further weight to the previous claim that PFN is a rare relaxor multiferroic.

As shown in Figure 6.6, peak at short r show higher temperature dependence and not matched well with no local structure model. So we fitted local structure for the r range between 1 to 10 Å.

Having concluded that the simplistic model A does not adequately explain even the high-temperature local structure, we now consider other models which might describe the data at all temperatures. Given lead's large thermal parameter even after accounting for the offset between the Pb and Fe/Nb sublattices in the Cm structure (model A) as shown in Fig. 6.5(d), it is natural to think of further Pb displacements as an origin of short-range structure as is often the case in closely related Pb-containing perovskite systems [50, 69] and as considered previously [54]. At 62 K, model B requires that the lead atoms shift by (−0.019,0.03,0.012) in fractions of the pseudocubic unit cell, less than previously reported [54]. Moving the Pb atoms introduces several peaks between $r = 3$ and $r = 4$ Å but their intensities are much smaller than in the experimental results, and the peak at $r = 2.5$ Å is not reproduced. Above the ferroelectric transition, symmetry constrains the Pb displacement to be (η, η, η), where $\eta = 0.02$ at 453 K. Displacing the Pb atoms in concert, which preserves the unit cell, is quite a simplistic model, and allowing the Pb atoms more freedom of movement should better model the real system. Accordingly, model C was introduced with the possibility of random shifts in the Pb positions.

Model C simulates the effect of Pb disorder using a $4 \times 4 \times 4$ supercell, in which each lead atom was allowed to move freely from its original position. Although this model was able to better model the ex-

perimental radial distribution function, at least at low temperatures, the average Pb displacement from its already displaced Cm position is 0.2 Å in this model. This is very large compared to Pb's atomic thermal motion in Fig. 6.5(d), approaches the upper limit observed in the strongest Pb-based ferroelectrics and $BiFeO_3$ with one of the highest polarization values of $\sim 86\,\mu C/cm^2$ [65], and would suggest an electric polarization far exceeding that reported [41, 42]. The comparative success of model C relative to model B is most likely a result of the significantly higher number of free parameters. Although model C is ruled out on the basis of the extremely large displacements compared to the reported polarization values, the fact that it required unphysical displacements of Pb implies that other atoms must also be considered. It has already been shown that the Fe/Nb atoms do not exhibit any significant displacement from their ideal positions [54]. That leaves oxygen, which has a larger thermal parameter and which is well known to depart from its ideal position in most perovskite structures, including in several Pb-containing phases which exhibit oxygen displacement [70–72] or the random rotation of oxygen polyhedra [3]. Model D allows the oxygen atoms to shift.

A further justification for considering O disorder comes from the reported random distribution of neighboring Fe^{3+} and Nb^{5+} [45] and the lack of any features in our data that would suggest even short-range cation order. The magnetic moments calculated from the long-range refinement are $3.4(6)\,\mu_B$ at 62 K (NOVA) and $3.3(3)\,\mu_B$ at 10 K (S-HRPD), corresponding to the high spin state of Fe^{3+}, which would make the two cations' sizes essentially identical and eliminate the common source of disorder. The next most probable reason for oxygen atoms to depart from their ideal positions is the displacements of the Pb^{2+} cations from their already-shifted positions, which would be expected to cause small rotations of the $(Fe,Nb)O_6$ octahedra. This would be frustrated, unless the Pb displacements ordered in one of a few very specific ways which would be expected to produce additional nuclear reflections. An orthogonal possibility arises from the electric-field gradients created by having a random distribution of Fe^{3+} and Nb^{5+} cations. An oxygen atom situated between an iron and a niobium site feels an electric-field gradient that will polarize it. Meanwhile, Nb^{5+}, having the electronic configuration of krypton,

will be unable to share electron density with oxygen, which $3d^5$ Fe^{3+} can, using its weakly antibonding e_g^* orbitals. In fact, iron, being a $3d$ transition metal, should have significant on-site electron repulsion and may benefit by donating some of its electron density to its oxygen ligands. All of these electronic effects would produce a net flow of electron density away from iron sites and toward niobium sites with many oxygen atoms caught in the middle. In model D, we combined lead displacement (model B) with oxygen disorder using a $4 \times 4 \times 4$ supercell. Here we allowed oxygen atoms to move freely while all lead atoms were constrained to move together. As one can see in Figs. 6.8(a) and 6.8(b), this model apparently fits the experimental results very well. The fitted atomic displacement in fractions of the pseudocubic unit cell for lead is (0.010,−0.004,0.008) at 62 K and (−0.0051) at 453 K, which is reduced compared to model B. For oxygen, the average shifts relative to the original site are (0.0195) at 62 K and (0.0203) at 453 K in fractional coordinates, which is around 0.08 Å. As is clear in Fig. 6.8, of the models considered here, model D is the most successful at describing the experimental results, and it does so in a physically reasonable manner.

In Fig. 6.9, we deconvoluted the contributions of correlations from each pair of atoms using models A and D for the 62 and 453 K data shown in Fig. 6.8. In each panel, the top six lines show correlation functions between individual pairs of atoms as labeled. Below this are the experimental results and best fit and finally the residuals. A comparison of panels (a) with (b) in Fig. 6.9 reveals that O–O correlations develop a great deal of additional structure at both temperatures, explaining well the additional peaks at $r = 2.5$–4 Å.

6.5 Summary

In conclusion, we have undertaken both high-resolution powder-diffraction and total scattering experiments on PFN in order to shed light on the unusual relaxor multiferroicity in this material. We focus on four key aspects of the physical properties: (i) determination of the low-temperature structure, (ii) the experimental examination of the reported negative thermal expansion behavior, (iii) possible structural evidence of mag-

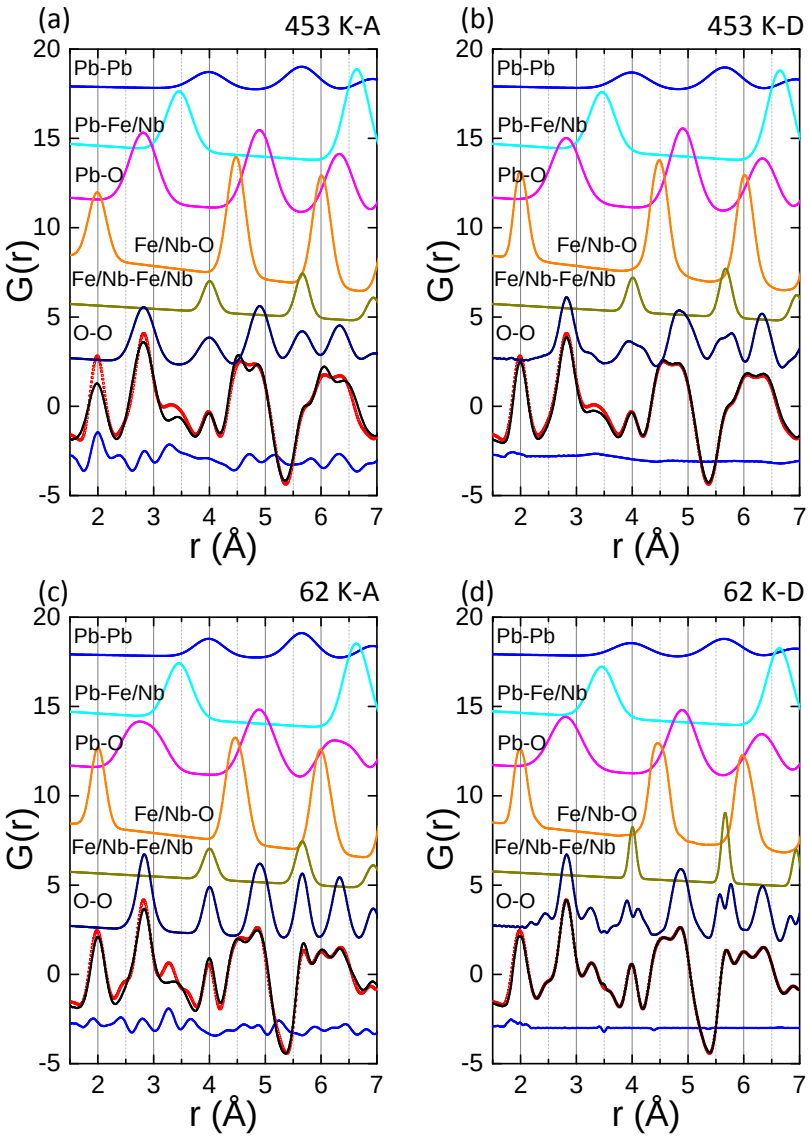

Figure 6.9: Atomic position correlations at 453 K and 62 K with (a) [(c)] no local structure and (b) [(d)] both Pb displacement and O disorder. The top six lines show atom-atom radial correlation functions as labeled, followed by the experimental results (circles), best fit (line), and finally its residuals (bottom line). Traces have been offset vertically for clarity.

netoelectric coupling, and (iv) the nature of the relaxor behavior. By combining both long- and short-range diffraction data, it is possible to provide new insight on each of the four issues. First, the high-resolution neutron-diffraction data are more consistent with the Cm space group at low temperatures as reported based on synchrotron data [49] and exclude the previously proposed $R3m$ [45] structure. However, there are no signs of the negative thermal expansion reported in Ref. [49] with the data instead being well fit by the conventional Debye-Grüneisen formula. We succeeded in finding a structural signature of the magnetoelectric coupling by Ginzburg-Landau analysis of the calculated electric polarization. Finally, the data clearly show that over the entire temperature range covered in this study there exists a short-range structure in addition to the global structure of $Pm\bar{3}m$ or Cm. This local structure occurs through Pb displacement as well as O disorder. That this local structure is present in PFN, even in the paraelectric phase, as seen in relaxor ferroelectric materials may hold the key to the strong frequency dependence seen in the dielectric constant of PFN. The results were published in ref. [28].

7. Summary and Outlook

7.1 Summary

Multiferroic materials are materials with more than one order parameter, and I studied on multiferroic materials with ferroelectricirty and magnetism by means of structural analysis. In hexagonal manganite $RMnO_3$, by determining that the peak intensity depends on the temperature, it was confirmed that the transition is mainly driven by R-O_P displacement, which is then accompanied by the MnO_5 tilting mode and the polarization mode, which vary more slowly. In $YMn_{1-x}(Al/Ga)_xO_3$, doping with Al or Ga of Mn sites reduces the ferroelectricity and transition temperature and changes the transition to the second order type from the weak first order type as the doping ratio is increased. Moreover, in $YMn_{1-x}(Al/Ga)_xO_3$, non-magnetic impurities on a 2D triangular lattice affect several physical properties, including the magnetization and heat capacity. Finally, we determined the structure of $Pb(Fe_{0.5}Nb_{0.5})O_3$ as the Cm structure and found Pb displacement with oxygen disorders using both long range and local structure studies. From these results, new methods of structural analysis were suggested. A structure analysis is an important tool in the study of multiferroic materials given that this methods can analyze atom movements using peak intensity, and determine the space group using the peak width change depending on the temperature.

7.2 Outlook

The suggested new structural analysis method can be applied to other systems in addition to hexagonal manganite. Here, I demonstrate the example of the structural transition processes of the perovskite structure materials, $LaMnO_3$ and $LaFeO_3$.

$LaMnO_3$ undergoes a structural transition from the cubic $Pm\bar{3}m$ structure to the orthogonal $Pnma$ structure. The d opbitals of Mn orders during the structural transition, and there have been reports of the existence of an intermediate rhombohedral ($R3c$) phase and those that

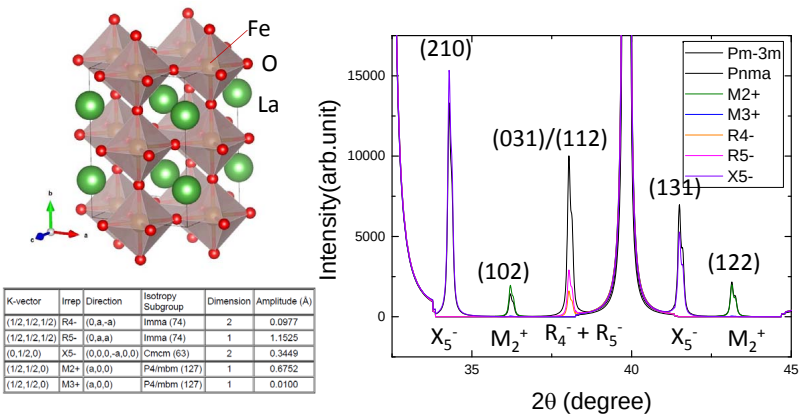

K-vector	Irrep	Direction	Isotropy Subgroup	Dimension	Amplitude (Å)
(1/2,1/2,1/2)	R4-	(0,a,-a)	Imma (74)	2	0.0977
(1/2,1/2,1/2)	R5-	(0,a,a)	Imma (74)	1	1.1525
(0,1/2,0)	X5-	(0,0,0,-a,0,0)	Cmcm (63)	2	0.3449
(1/2,1/2,0)	M2+	(a,0,0)	P4/mbm (127)	1	0.6752
(1/2,1/2,0)	M3+	(a,0,0)	P4/mbm (127)	1	0.0100

Figure 7.1: Simulation of the structural transition of $LaFeO_3$

did not find this phase [73, 74]. This d-orbital ordering is also highly correlated with the C-type antiferromagnetic structure.

$LaFeO_3$ also undergoes a structural transition similar to $LaMnO_3$. It also has a G-type antiferromagnetic transition around 760 K, a considerably high temperature. It has ferromagnetism due to the canting of the magnetic moment direction. It has basically a paraelectric orthogonal $Pnma$ structure, but due to the tilting and distortion of the polyhedral, there are D-M interactions and reports on ferroelectric properties as well [75, 76].

As noted above, both materials undergo a structural transition from the cubic $Pm\bar{3}m$ structure to the orthogonal $Pnma$ structure, and the simulation patterns are fundamentally similar with only a difference in the intensity levels. Figure 7.1 shows the simulation pattern associated with each mode between the cubic and orthogonal $LaFeO_3$. Each peaks is indexed to each mode, in the case the (210) peak to the X_5^- mode and the (102) peak to the M_2^+ mode. We can track the movements of atoms by tracking these peaks and can thus understand how these movements affect on the structural transition process.

In addition to the materials discussed above, this new method can easily be applied to other systems which undergo structural transitions with the appearance of new peaks due to breaking of symmetry or the growth of unit cells. It would be useful on study on this structural transition process and ferroelectricity itself.

References

[1] C. Guguschev, J. Götze, and M. Göbbels, American Mineralogist **95**, 449 (2010).

[2] T. E. Mason, Physics Today **59**, 44 (2006).

[3] T. Egami, E. Mamontov, W. Dmowski, and S. B. Vakhrushev, AIP Conf. Proc. **677**, 48 (2003).

[4] E. Borfecchia, C. Garino, L. Salassa, and C. Lamberti, Phil. Trans. R. Soc. A **371**, 20120132 (2013).

[5] C. L. Farrow, P. Juhas, J. W. Liu, D. Bryndin, E. S. Bozin, J. Bloch, T. Proken, and S. J. L. Billange, J. Phys.: Condens. Matter **19**, 335219 (2007).

[6] N. Hill *et al.*, Journal of Physical Chemistry B **104**, 6694 (2000).

[7] T. Choi, Y. Horibe, H. Yi, Y. Choi, W. Wu, and S. Cheong, Nature materials **9**, 253 (2010).

[8] S. Kim, S. Lee, T. Kim, T. Zyung, Y. Jeong, and M. Jang, Crystal Research and Technology **35**, 19 (2000).

[9] B. B. Van Aken, T. T. Palstra, A. Filippetti, and N. A. Spaldin, Nature materials **3**, 164 (2004).

[10] S. Lee, A. Pirogov, M. Kang, K.-H. Jang, M. Yonemura, T. Kamiyama, S. Cheong, F. Gozzo, N. Shin, H. Kimura, *et al.*, Nature **451**, 805 (2008).

[11] J. Oh, M. D. Le, H.-H. Nahm, H. Sim, J. Jeong, T. Perring, H. Woo, K. Nakajima, S. Ohira-Kawamura, Z. Yamani, *et al.*, Nature Communications **7**, 13416 (2016).

[12] K. Łukaszewicz and J. Karut-Kalicińska, Ferroelectrics **7**, 81 (1974).

[13] H. Sim, J. Oh, J. Jeong, M. D. Le, and J.-G. Park, Acta Crystallographica Section B: Structural Science, Crystal Engineering and Materials **72**, 3 (2016).

[14] H. T. Stokes and D. M. Hatch, *Isotropy subgroups of the 230 crystallographic space groups* (World Scientific, Singapore, 1988).

[15] T. Lonkai, D. Tomuta, U. Amann, J. Ihringer, R. Hendrikx, D. Többens, and J. Mydosh, Physical Review B **69**, 134108 (2004).

[16] S.-Z. Lin, X. Wang, Y. Kamiya, G.-W. Chern, F. Fan, D. Fan, B. Casas, Y. Liu, V. Kiryukhin, W. H. Zurek, C. D. Batista, and S.-W. Cheong, Nature Physics **10**, 970 (2014).

[17] C. J. Fennie and K. M. Rabe, Physical Review B **72**, 100103 (2005).

[18] J. Kim, K. C. Cho, Y. M. Koo, K. P. Hong, and N. Shin, Applied Physics Letters **95**, 132901 (2009).

[19] G. Nénert, M. Pollet, S. Marinel, G. Blake, A. Meetsma, and T. T. Palstra, J. Phys.: Condens. Matter **19**, 466212 (2007).

[20] S. Abrahams, Acta Crystallographica Section B: Structural Science **65**, 450 (2009).

[21] I.-K. Jeong, N. Hur, and T. Proffen, Journal of Applied Crystallography **40**, 730 (2007).

[22] T. Tyson, T. Wu, H. Chen, J. Bai, K. Ahn, K. Pandya, S. Kim, and S.-W. Cheong, Journal of Applied Physics **110**, 084116 (2011).

[23] A. S. Gibbs, K. S. Knight, and P. Lightfoot, Physical Review B **83**, 094111 (2011).

[24] M. Lilienblum, T. Lottermoser, S. Manz, S. M. Selbach, A. Cano, and M. Fiebig, Nature Physics **11**, 1070 (2015).

[25] J. Rodríguez-Carvajal, Physica B **192**, 55 (1993).

[26] D. Orobengoa, C. Capillas, M. I. Aroyo, and J. M. Perez-Mato, Journal of Applied Crystallography **42**, 820 (2009).

[27] S. Chae, N. Lee, Y. Horibe, M. Tanimura, S. Mori, B. Gao, S. Carr, and S.-W. Cheong, Physical Review Letters **108**, 167603 (2012).

[28] H. Sim, D. C. Peets, S. Lee, S. Lee, T. Kamiyama, K. Ikeda, T. Otomo, S.-W. Cheong, and J.-G. Park, Physical Review B **90**, 214438 (2014).

[29] S. Abrahams, Acta Crystallographica Section B: Structural Science **57**, 485 (2001).

[30] S. Choi, H. Sim, S. Kang, K.-Y. Choi, and J.-G. Park, J. Phys.: Condens. Matter **29**, 095602 (2017).

[31] S. M. Griffin, M. Reidulff, S. M. Selbach, and N. A. Spaldin, Chemistry of Materials **29**, 2425 (2017).

[32] J. Park, M. Kang, J. Kim, S. Lee, K.-H. Jang, A. Pirogov, J.-G. Park, C. Lee, S.-H. Park, and H. C. Kim, Physical Review B **79**, 064417 (2009).

[33] A. R. Damodaran, E. Breckenfeld, Z. Chen, S. Lee, and L. W. Martin, Advanced Materials **26**, 6341 (2014).

[34] A. Wollny, L. Fritz, and M. Vojta, Physical Review Letters **107**, 137204 (2011).

[35] V. Maryasin and M. Zhitomirsky, Physical Review Letters **111**, 247201 (2013).

[36] H. Zhou, J. Denyszyn, and J. Goodenough, Physical Review B **72**, 224401 (2005).

[37] H. Zhou, J. Janik, B. Vogt, Y. Jo, L. Balicas, M. Case, C. Wiebe, J. Denyszyn, J. Goodenough, and J. Cheng, Physical Review B **74**, 094426 (2006).

[38] A. Nugroho, N. Bellido, U. Adem, G. Nénert, C. Simon, M. Tjia, M. Mostovoy, and T. Palstra, Physical Review B **75**, 174435 (2007).

[39] S.-W. Cheong and M. Mostovoy, Nature Mater. **6**, 13 (2007).

[40] M. Fiebig, J. Phys. D **38**, R123 (2005).

[41] A. Kania, E. Talik, and M. Kruczek, Ferroelectrics **391**, 114 (2009).

[42] R. K. Mishra, R. N. P. Choudhary, and A. Banerjee, J. Phys.: Condens. Matter **22**, 025901 (2010).

[43] V. V. Laguta, M. D. Glinchuk, M. Maryško, R. O. Kuzian, S. A. Prosandeev, S. I. Raevskaya, V. G. Smotrakov, V. V. Eremkin, and I. P. Raevski, Physical Review B **87**, 064403 (2013).

[44] J. T. Wang, C. Zhang, Z. X. Shen, and Y. Feng, Ceramics Int. **30**, 1627 (2004).

[45] S. A. Ivanov, R. Tellgren, H. Rundlof, N. W. Thomas, and S. Ananta, J. Phys.: Condens. Matter **12**, 2393 (2000).

[46] E. I. Sitalo, Y. N. Zakharov, A. G. Lutokhin, S. I. Raevskaya, I. P. Raevski, M. S. Panchelyuga, V. V. Titov, L. E. Pustovaya, I. N. Zakharchenko, A. T. Kozakov, and A. A. Pavelko, Ferroelectrics **389**, 107 (2009).

[47] B. Fraygola, N. Frizon, M. H. Lente, A. A. Coelho, D. Garcia, and J. A. Eiras, Integrated Ferroelectrics: An International Journal **124**, 53 (2011).

[48] M. H. Lente, J. D. S. Guerra, G. K. S. de Souza, B. M. Fraygola, C. F. V. Raigoza, D. Garcia, and J. A. Eiras, Physical Review B **78**, 054109 (2008).

[49] S. P. Singh, D. Pandey, S. Yoon, S. Baik, and N. Shin, Applied Physics Letters **90**, 242915 (2007).

[50] N. Lampis, P. Sciau, and A. G. Lehmann, J. Phys.: Condens. Matter **11**, 3489 (1999).

[51] P. M. Woodward, Acta. Cryst. B **53**, 32 (1997).

[52] I. G. Wood, K. S. Knight, G. D. Price, and J. A. Stuart, J. Appl. Cryst. **35**, 291 (2002).

[53] A. Mesquita, B. M. Fraygola, V. R. Mastelaro, and J. A. Eiras, Applied Physics Letters **100**, 172907 (2012).

[54] I.-K. Jeong, J. S. Ahn, B. G. Kim, S. Yoon, S. P. Singh, and D. Pandey, Physical Review B **83**, 064108 (2011).

[55] R. Kolesova and M. Kupriyanov, Phase Transitions **45**, 271 (1993).

[56] Y. X. Wang, W. L. Zhong, C. L. Wang, and P. L. Zhang, Phys. Lett. A **288**, 45 (2001).

[57] I.-K. Jeong and S. Park, J. Korean Phys. Soc. **59**, 2756 (2011).

[58] R. Kolesova, V. Kolesov, M. Kupriyanov, and R. Skulski, Phase Transitions **68**, 621 (1999).

[59] S. Lee, J. R. Zhang, S. Torii, S. Choi, D.-Y. Cho, T. Kamiyama, J. Yu, K. A. McEwen, and J.-G. Park, J. Phys.: Condens. Matter **25**, 465601 (2013).

[60] A. Y. Wu and R. J. Sladek, Physical Review B **27**, 2089 (1983).

[61] S. Lee, J.-G. Park, D. T. Adroja, D. Khomskii, S. Strelsov, K. A. McEwen, H. Sakai, K. Yoshimura, V. I. Anisimov, D. Mori, R. Kanno, and R. Ibberson, Nature Mater. **5**, 471 (2006).

[62] J. Park, S. Lee, M. Kang, K.-H. Jang, C. Lee, S. V. Streltsov, V. V. M. M. V. Valentyuk, J. E. Medvedeva, T. Kamiyama, and J.-G. Park, Physical Review B **82**, 054428 (2010).

[63] D. P. Kozlenko, S. E. Kichanov, S. Lee, J.-G. Park, V. P. Glazkov, and B. N. Savenko, JETP Lett. **82**, 193 (2005).

[64] D. Andrault, N. Bolfan-Casanova, and N. Guignot, Earth Planet. Sci. Lett. **193**, 501 (2001).

[65] S. Lee, M. T. Fernandez-Diaz, H. Kimura, Y. Noda, D. T. Adroja, S. Lee, J. Park, V. Kiryukhin, S.-W. Cheong, M. Mostovoy, and J.-G. Park, Physical Review B **88**, 060103(R) (2013).

[66] R. D. King-Smith and D. Vanderbilt, Physical Review B **47**, 1651(R) (1993).

[67] T. Egami and S. J. L. Billinge, *Underneath The Bragg Peaks: Structural Analysis of Complex Materials* (Pergamon, New york, 2003) Chap. Magnetic Correlation Functions.

[68] I.-K. Jeong, T. W. Darling, J. K. Lee, T. Proffen, R. H. Heffner, J. S. Park, K. S. Hong, W. Dmowski, and T. Egami, Physical Review Letter **94**, 147602 (2005).

[69] C. Malibert, B. Dkhil, J. M. Kiat, D. Durand, J. F. Bérar, and A. S. de Biré, J. Phys.: Condens. Matter **9**, 7485 (1997).

[70] W. Dmowski, M. K. Akbas, P. K. Davies, and T. Egami, J. Phys. Chem. Solids **61**, 229 (2000).

[71] G. Baldinozzi, P. Sciau, and J. Lapasset, Phys. Status Solidi A **133**, 17 (1992).

[72] I. W. Chen, J. Phys. Chem. Solids **61**, 197 (2000).

[73] J. Rodriguez-Carvajal, M. Hennion, F. Moussa, A. Moudden, L. Pinsard, and A. Revcolevschi, Physical Review B **57**, R3189 (1998).

[74] T. Chatterji, F. Fauth, B. Ouladdiaf, P. Mandal, and B. Ghosh, Physical Review B **68**, 052406 (2003).

[75] S. A. Ivanov, R. Tellgren, F. Porcher, T. Ericsson, A. Mosunov, P. Beran, S. Korchagina, P. A. Kumar, R. Mathieu, and P. Nordblad, Materials Research Bulletin **47**, 3253 (2012).

[76] S. Acharya, J. Mondal, S. Ghosh, S. Roy, and P. Chakrabarti, Materials Letters **64**, 415 (2010).

Publications

1. **Studies on the high-temperature ferroelectric transition of multiferroic hexagonal manganite $RMnO_3$**
   Hasung Sim, Jaehong Jeong, Haeri Kim, S-W Cheong, and Je-Geun Park
   J. Phys.: Condens. Matter Under Review (2018)

2. **Frustrated antiferromagnetic honeycomb-tunnel-like lattice $CuR_2Ge_2O_8$ (R = Pr, Nd, Sm, and Eu)**
   Hwanbeom Cho, Marie Kratochvílová, Nahyun Lee, Hasung Sim, and Je-Geun Park
   Physical Review B **96**, 224427 (2017)

3. **Properties of spin-1/2 triangular-lattice antiferromagnets $CuY_2Ge_2O_8$ and $CuLa_2Ge_2O_8$**
   Hwanbeom Cho, Marie Kratochvílová, Hasung Sim, Ki-Young Choi, Choong Hyun Kim, Carley Paulsen, Maxim Avdeev, Darren C. Peets, Younghun Jo, Sanghyun Lee, Yukio Noda, Michael J. Lawler, and Je-Geun Park
   Physical Review B **95**, 144404 (2017)

4. **Spin glass behavior in frustrated quantum spin system $CuAl_2O_4$ with a possible orbital liquid state**
   R Nirmala, Kwang-Hyun Jang, Hasung Sim, Hwanbeom Cho, Junghwan Lee, Nam-Geun Yang, Seongsu Lee, R M Ibberson, K Kakurai, M Matsuda, S-W Cheong, V V Gapontsev, S V Streltsov and Je-Geun Park
   J. Phys.: Condens. Matter **29**, 13LT01 (2017)

5. **Doping effects on trimerization and magnetoelectric coupling of single crystal multiferroic (Y,Lu)MnO_3**
   Seongil Choi, Hasung Sim, Soonmin Kang, Ki-Young Choi and Je-Geun Park

J. Phys.: Condens. Matter **29**, 095602 (2017)

6. **Magnetic transitions in the chiral armchair-kagome system $Mn_2Sb_2O_7$**
   Darren C. Peets, Hasung Sim, Seongil Choi, Maxim Avdeev, Seongsu Lee, Su Jae Kim, Hoju Kang, Docheon Ahn, and Je-Geun Park
   Physical Review B **95**, 14424 (2017)

7. **Spontaneous structural distortion of the metallic Shastry-Sutherland system DyB_4 by quadrupole-spin-lattice coupling**
   Hasung Sim, Seongsu Lee, Kun-Pyo Hong, Jaehong Jeong, J. R. Zhang, T. Kamiyama, D. T. Adroja, C. A. Murray, S. P. Thompson, F. Iga, S. Ji, D. Khomskii, and Je-Geun Park
   Physical Review B **94**, 195128 (2016)

8. **Hexagonal $RMnO_3$: a model system for two dimensional triangular lattice antiferromagnets**
   Hasung Sim, Joosung Oh, Jaehong Jeong, Manh Duc Le and Je-Geun Park
   Acta Crystallographica Section B **72**, 3 (2016)

9. **3d-electron Heisenberg pyrochlore $Mn_2Sb_2O_7$**
   Darren C. Peets, Hasung Sim, Maxim Avdeev, and Je-Geun Park
   Physical Review B **94**, 174431 (2016)

10. **Spontaneous decays of magneto-elastic excitations in non-collinear antiferromagnet (Y,Lu)MnO_3**
    Joosung Oh, Manh Duc Le, Ho-Hyun Nahm, Hasung Sim, Jaehong Jeong, T.G. Perring, Hyungje Woo, Kenji Nakajima, Seiko Ohira-Kawamura, Zahra Yamani, Y. Yoshida, H. Eisaki, S.-W. Cheong, A. L. Chernyshev and Je-Geun Park
    Nature Communications **7**, 13146 (2016)

11. **Robust singlet dimers with fragile ordering in two-dimensional honeycomb lattice of Li_2RuO_3**
Junghwan Park, Teck-Yee Tan, D. T. Adroja, A. Daoud-Aladine, Seongil Choi, Deok-Yong Cho, Sang-Hyun Lee, Jiyeon Kim, Hasung Sim, T. Morioka, H. Nojiri, V. V. Krishnamurthy, P. Manuel, M. R. Lees, S. V. Streltsov, D. I. Khomskii and Je-Geun Park
Scientific Reports **6**, 25238 (2016)

12. **High-resolution structure studies and magnetoelectric coupling of relaxor multiferroic $Pb(Fe_{0.5}Nb_{0.5})O_3$**
Hasung Sim, Darren C. Peets, Sanghyun Lee, Seongsu Lee, T. Kamiyama, K. Ikeda, T. Otomo, S.-W. Cheong, and Je-Geun Park
Physical Review B **90**, 214438 (2014)

13. **Low Temperature Measurement of the Electrical Conductivity in Amorphous InGaZnO Thin Films**
Hasung Sim,Seongil Choi, Je-Geun Park, Jaewon Song, Seungwu Han, Cheol Seong Hwang, and Deok-Yong Cho
ECS Journal of Solid State Science and Technology **3**, (2) P10–P12 (2014)

14. **The impact of orbital hybridization on the electronic structure of crystalline InGaZnO: a new perspective on the compositional dependence**
Youngho Kang, Sanghyun Lee, Hasung Sim, Chang Hee Sohn, Won Goo Park, Seul Ji Song, Un Ki Kim, Cheol Seong Hwang, Seungwu Han and Deok-Yong Cho
J. Mater. Chem. C **2**, 9196 (2014)

15. **Analysis of the One-dimensional Yut-Nori Game: Winning Strategy and Avalanche-size Distribution**
Hye Jin Park Hasung Sim,Hang-Hyun Jo and Beom Jun Kim
Journal of the Korean Physical Society **63**, 8 (2013)

16. **Antiferromagnetic ordering in Li_2MnO_3 single crystals with a two-dimensional honeycomb lattice**
Sanghyun Lee, Seongil Choi, Jiyeon Kim, Hasung Sim, Choongjae Won, Seongsu Lee, Shin Ae Kim, Namjung Hur and Je-Geun Park
J. Phys.: Condens. Matter **24**, 456004 (2012) IOP select

Conference Presentations
(Oral presentations)

1. **Single ferroelectric transition of weak first-order in multiferroic hexagonal manganite $RMnO_3$**
2017 Materials Research Society fall meeting & exhibit (Nov. 2017 in USA)

2. **Single ferroelectric transition of weak first-order in multiferroic hexagonal manganite $RMnO_3$**
2017 Korean Physical Society fall meeting (Oct. 2017 in Korea)

3. **High-resolution structure studies and magnetoelectric coupling of relaxor multiferroic $Pb(Fe_{0.5}Nb_{0.5})O_3$**
2014 Korean Physical Society fall meeting (Oct. 2014 in Korea)

(Poster presentations)

1. **Doping effects on 2D triangular multiferroic $Y(Mn,Al,Ga)O_3$**
APCTP-Quantum Materials Symposium 2017 (Feb. 2017 in Korea)

2. **Doping effects on 2D triangular multiferroic $Y(Mn, Al)O_3$**
The Gordon Research Conference on Correlated Electron Systems (Aug. 2016 in USA)

3. **High-resolution structure studies and magnetoelectric coupling of relaxor multiferroic Pb($Fe_{0.5}Nb_{0.5}$)O_3**
   CIFAR Quantum Materials Summer School 2015 (May. 2015 in Canada)

4. **High-resolution structure studies and magnetoelectric coupling of relaxor multiferroic Pb($Fe_{0.5}Nb_{0.5}$)O_3**
   15th Taiwan-Japan-Korea Symposium on Strongly Correlated Electron Systems (Mar. 2015 in Taiwan)

5. **High-resolution structure studies and magnetoelectric coupling of relaxor multiferroic Pb($Fe_{0.5}Nb_{0.5}$)O_3**
   The International Conference on Strongly Correlated Electron Systems (SCES 14) (Oct. 2014 in France)

6. **Long- and Short-Ranged Structure of Multiferroic Pb($Fe_{0.5}Nb_{0.5}$)O_3**
   The 7th Asia Oceania Forum for Synchrotron Radiation Research (Sep. 2013 in Japan)

7. **Long- and Short-Ranged Structure of Multiferroic Pb($Fe_{0.5}Nb_{0.5}$)O_3**
   International Conference on Neutron Scattering (Jul. 2013 in UK)

8. **Long- and Short-Ranged Structure of Multiferroic Pb($Fe_{0.5}Nb_{0.5}$)O_3**
   2013 Korean Physical Society spring meeting (Apr. 2013 in Korea)

9. **Spontaneous distortion of Shastry-Sutherland lattice by spin-lattice-quadrupole coupling in DyB_4**
   Quantum Materials Symposium (QMS) (Mar. 2013 in Korea)

10. **Spontaneous distortion of Shastry-Sutherland lattice by spin-lattice-quadrupole coupling in DyB_4**
    The 13th Japan-Korea-Taiwan Symposium on Strongly correlated

Electron Systems (Jan. 2013 in Japan)

11. **Composition-dependent electrical conduction in amorphous InGaZnO thin films at low temperatures**
6th BK 21 Young Physists Workshop (Dec. 2012 in Korea)

12. **Composition-dependent electrical conduction in amorphous InGaZnO thin films at low temperatures**
The 4th ATCTP-IACS Joint Conference on physics of novel and emerging materials (Oct. 2012 in Korea)

국문초록

다중강성 물질의 구조연구: 육방정계 망간산화물과 $PbFe_{0.5}Nb_{0.5}O_3$

심하성
물리천문학부 물리학전공
서울대학교 대학원

강유전성과 강자성을 동시에 띠는 물질인 다중강성 물질 중 육방정계 망간산화물 ($RMnO_3$) 과 $PbFe_{0.5}Nb_{0.5}O_3$의 특성을 구조분석을 통하여 분석하였다. $RMnO_3$는 독특한 2차원 삼각격자 구조를 가지고 있는데, 이 물질의 상유전의 $P6_3/mmc$ 구조에서 강유전의 $P6_3cm$ 구조로의 구조 상전이 과정을 연구하였다. 이 때 기존의 Rietveld 분석 과정이 아니라 픽의 세기를 이용한 모드 분석을 통해 이 구조상전이는 중간에 다른 상이 없는 하나의 상전이이며, R-O_P변위 가 1차 상전이 행동을 보이고, MnO_5 틀어짐 모드나 극성 모드는 2차 상전이 행동을 보임을 밝혔다. 또한 이 육방정계 망간산화물 중 $YMnO_3$에 자성이온인 Mn 자리에 이온 크기가 작고 비자성 이온인 Al과 Ga 이온을 첨가하여 구조 상전이 과정에의 변화와 자기 특성의 변화를 살펴보았다. 1차 상전이 행동을 보이던 R-O_P변위 모드는 Al 이온의 첨가 비율이 증가함에 따라 점점 더 2차 상전이 처럼 연속적으로 변화한다. 이는 Al 이온이 Mn 이온보다 크기가 작기 때문에 국조적인 변형이 일어나서로 추정된다. 그리고 Al 이온과 Ga 이온의 첨가로 인해 자기 상전이 온도가 감소하고, 저온에서 강자성 특성이 보이며, 저 에너지 들뜸이 존재한다. 그리고 페로보스카이트 구조의 $PbFe_{0.5}Nb_{0.5}O_3$ 물질은 고 분해능 중성자 회절실험과 총 산란 실험을 수행하였다. 구조 분석과정에서 픽 폭의 온도의존성 분석을 통해 구조를 Cm으로 명확히 밝히고, 국소 구조 연구를 통해 구조상전이 위의 온도에서도 납 원자의 변위와 산소원자의 무질서가 있음을 밝혔다. 이런 다중강성 물질들의 통합적인 연구를 통해 구조분석의 새로운 방법을 제시하였으며 이는 다른 다중강성 물질의 구조 연구에도 도움이 될 것이다.

주요어: 삼각격자 반강자성체, $RMnO_3$, $PbFe_{0.5}Nb_{0.5}O_3$
학 번: 2011-20408